NOTICE

The quality of this microform is heavily dependent upon the quality of the original thesis submitted for microfilming. Every effort has been made to ensure the highest quality of reproduction possible.

If pages are missing, contact the university which granted the degree.

Some pages may have indistinct print especially if the original pages were typed with a poor typewriter ribbon or if the university sent us an inferior photocopy.

Reproduction in full or in part of this microform is governed by the Canadian Copyright Act, R.S.C. 1970, c. C-30, and subsequent amendments.

AVIS

La qualité de cette microforme dépend grandement de la qualité de la thèse soumise au microfilmage. Nous avons tout fait pour assurer une qualité supérieure de reproduction.

S'il manque des pages, veuillez communiquer avec l'université qui a conféré le grade.

La qualité d'impression de certaines pages peut laisser à désirer, surtout si les pages originales ont été dactylographiées à l'aide d'un ruban usé ou si l'université nous a fait parvenir une photocopie de qualité inférieure.

La reproduction, même partielle, de cette microforme est soumise à la Loi canadienne sur le droit d'auteur, SRC 1970, c. C-30, et ses amendements subséquents.

Scattering of keV Ions from a Clean Silicon Single Crystal Surface

by

Pierre Gauthier

Thesis submitted to the School of Graduate Studies and Research in partial fulfillment of the requirements for the degree of Master of Science in Physics

Physics Department
Faculty of science
University of Ottawa
Ottawa, Canada

ISBN 0-315-75100-2

UNIVERSITÉ D'OTTAWA
UNIVERSITY OF OTTAWA

Abstract

An apparatus for measuring energy and angular distributions of keV ions forward scattered from atomically clean silicon surfaces was designed and assembled. A consistent procedure for cleaning Si(100) single crystal surfaces under ultra-high vacuum was established. Experimentally, oxygen ions were surface scattered from a clean Si(100) sample and the ratios of outgoing negative to positive ions were measured. By using a positive oxygen beam and then a negative oxygen beam we obtained strong evidence that ions retain no memory of their initial charge state after it undergoes a violent collision with a single atom. The ratios of negative to positive scattered oxygen ions for both an incident O^- ion beam and O^+ ion beam (under identical scattering conditions) were found to be the same (within statistical uncertainty) for incident energies between 6 keV and 20 keV.

Acknowledgements

I would like to express my sincere thanks to Dr. Brian Hird for the confidence and patience he showed and the time he spent with me throughout the past two years.

I would like to thank Dr. Robert A. Armstrong for his help with the samples and his meaningful insight into our field of research and also to John Bulicz whose help and cooperation proved invaluable during the last two years.

Many thanks to Bob Hart, Ron, Herve, Len and Francois, for all the excellent machining, shop work and loan of their tools. Thanks also to Art Buser and Mike Murphy in the electronic shop for their constructive advice and help.

Finally, I would like to express my deep appreciation to my parents, whose backing and support made this thesis possible.

Contents

List of Tables and Figures

CHAPTER 1 - Introduction

The scattering of ions from surfaces is a well established field of physics. In many cases it is studied to elucidate the structure of the surface involved. It is also used to detect effects related to the charge transfer occurring at the surface.

The application of low-energy ion scattering (LEIS) techniques to the study of the composition and structural arrangement of solid surfaces has developed considerably in the past few years [1]. The aim of these experiments was to obtain information about the scattering process, channeling and blocking effects and neutralisation processes. These processes and effects have recently been found to depend partly on the geometry of the atoms in the first few surface layers so that ion scattering is one of the techniques available to obtain structural information about surfaces. It complements the information from electron scattering in which a Fourier transform from momentum space is required.

For certain ranges of ion energies and scattering geometry, surface species can generally be identified by the presence of surface scattering peaks in the scattered ion energy spectrum and the surface concentration of these species can be related to the size of these peaks. The energies of scattered and recoiled particles can be predicted very accurately by using classical physics and describing the process as binary collisions between hard-spheres. Such a simple model is adequate for identifying spectral peaks; the analysis of multiple collision

trajectories and inelastic energy losses require more rigorous models.

The shadowing and blocking by nearby atoms of energetic ions that are scattered from single-crystal surfaces has been extensively developed as a crystallographic tool. This technique was used initially mainly at ion energies above about 50 keV where the cone angles are quite small, less than 5°. Recently interest in this technique has moved to the low-keV region partly because at low energies, the scattering measurement are more selective of the surface atom, particularly if neutral atoms as well as scattered ions are detected. More importantly, it has been realized that a consequence of the wider shadow-cone angles is that surface atoms pass in and out of the shadow of their immediate neighbors on the surface, and for incident-beam directions sufficiently far away from grazing incidence, surface roughness is not a serious problem [2,3,4].

CHAPTER 2 - Some theoretical aspects of ion scattering

2.1 Kinematics of the collision

When an energetic ion is scattered by a single atom its energy after the collision depends on the kinematics of the elastic collision and on the inelastic (electronic) energy losses. For primary energies in the keV range, the elastic energy loss is far greater than the inelastic energy losses which can be ignored. The observed peaks in the energy spectra of experimental surface scattering measurements are found to agree closely with the predictions of this simple two body process, so that it can be inferred that interactions between atoms in the surface can be neglected and the struck atom only shares its recoil energy after the collision. A quantum approach could also be used to analyse the collision but since the de Broglie wavelength is much smaller than the atom spacing, a simple classical approach is sufficient [5].

The wavelength for the corresponding wave is:

$$\lambda = \frac{h}{p} = \frac{h}{(2mE)^{1/2}}$$

where $p^2 = 2\ m\ E$ for a non-relativistic particle

Thus for 10 keV oxygen ions, $\lambda = 2.3 \times 10^{-3}$ Å compared to a typical atomic size and lattice spacing of a few Å.

The laws of conservation of energy and momentum can be used to describe scattered and recoiled particle trajectories and energies [6]. The energy of the scattered ions (E_s) or recoiled atoms (E_r) is entirely determined by the scattering angle θ in the

laboratory frame and the mass ratio A (= m_2 / m_1 or target mass/incident mass).

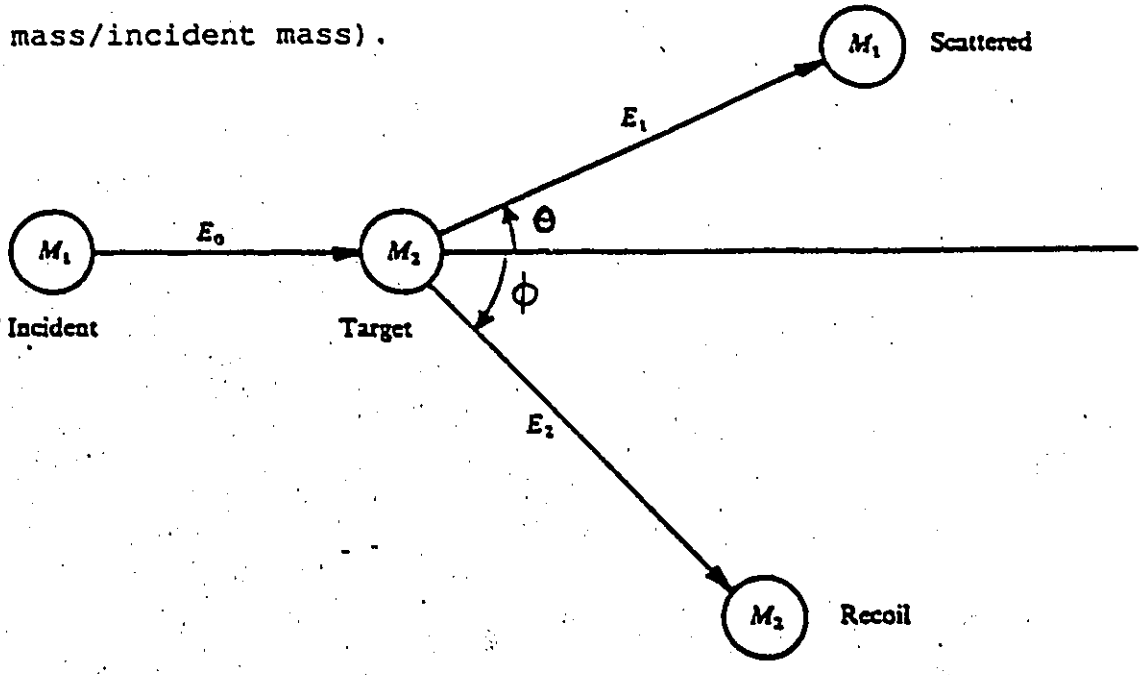

FIGURE #1a) Kinematic diagram of the scattering geometry

$$K_s = \frac{E_s}{E_o} = \left[\frac{\cos\theta \pm \sqrt{A^2 - (\sin\theta)^2}}{1 + A}\right]^2$$

$$K_r = \frac{E_r}{E_o} = \frac{4A\,(\cos\phi)^2}{(1 + A)^2}$$

where E_o is the incident ion energy and ϕ is the recoil angle. These two functions are plotted in FIGURE #1 b), c) for a few values of A.

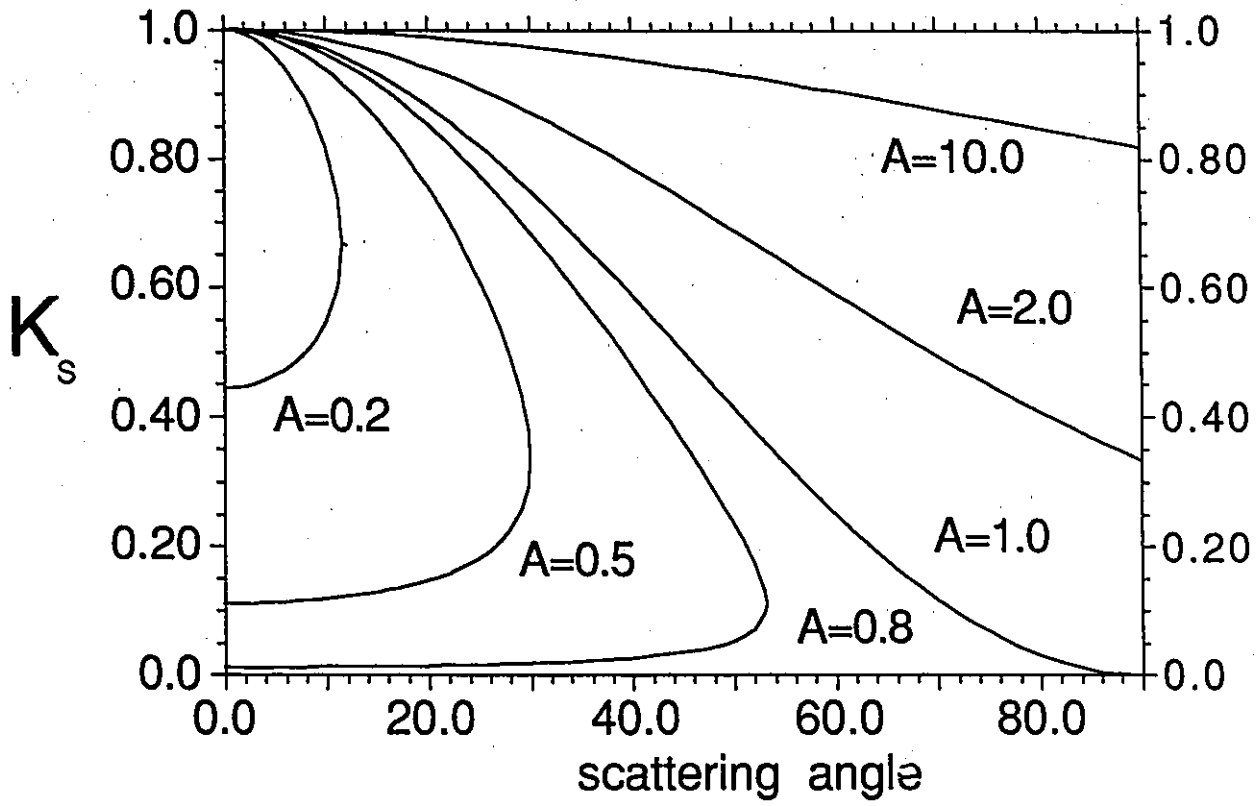

FIGURE #1 b) Kinematic curves for scattered atoms

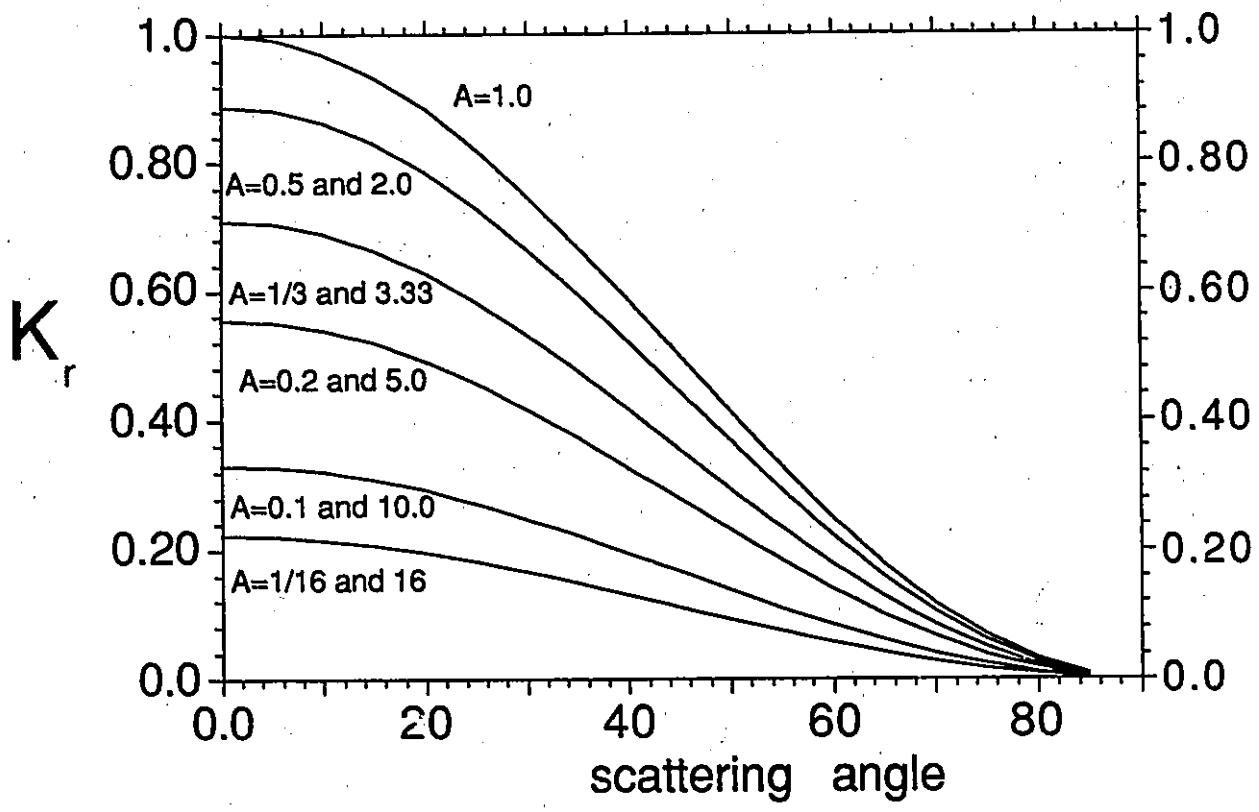

FIGURE #1 c) Kinematic curves for recoiled atoms

2.2 Shadowing and blocking

When an energetic ion hits an atom it will be deflected in another direction. Consequently when a well collimated ion beam is used there will be a resulting shadow cone behind each target atom which is inaccessible to the primary particles as illustrated in FIGURE #2.

For atomic collisions in the keV range, the force of interaction between two colliding particles is almost wholly repulsive and usually believed to be of the screened Coulomb type [7]. The screened Coulomb potential as in Rutherford scattering from an unscreened Coulomb potential produces mostly forward scattering. Backscattered involves only the small fraction of particles which have an impact parameter less than the Thomas-Fermi electron screening radius (e.g. for copper the screening length is 0.55 Å). Consequently, the backscattering yield is much smaller than the forward scattering yield.

In scattering experiments on single crystals, surface sensitivity is obtained by aligning the ion beam with a major crystal direction. FIGURE #3 shows a collection of computer-generated trajectories for an ion beam incident on a crystal along a low-index direction [8]. Note the development of shadows behind the surface atoms and a few small-impact parameter collisions leading to backscattering (the randomly oriented arrows). In an ideal static lattice, only the top layer atoms are then hit by the incident ion beam. The atoms further along the aligned atomic rows are located in the shadow and therefore cannot contribute to the

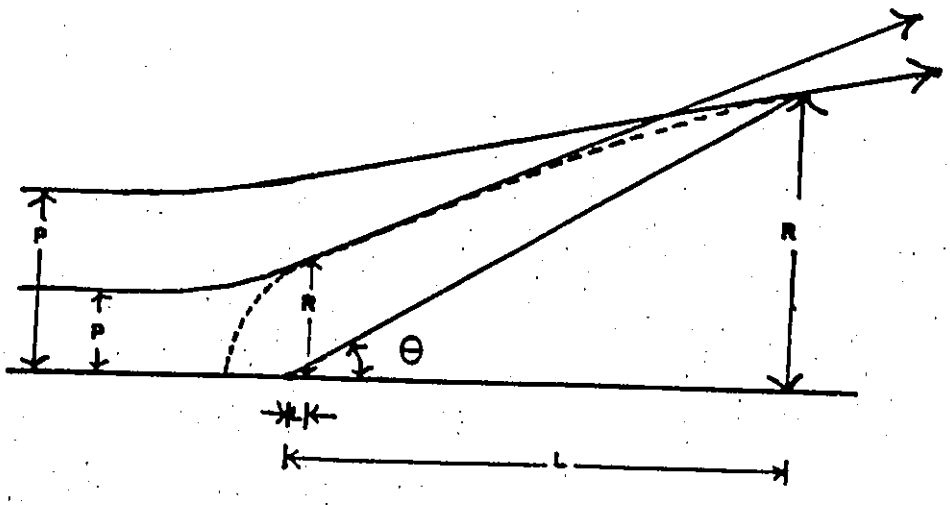

FIGURE #2 Formation of a shadow cone behind an atom. The dotted line shows the envelope formed by plotting all the deflected trajectories. Note that R is the radius of the cone cast over a point at a distance L from the target atom and P is the impact parameter.

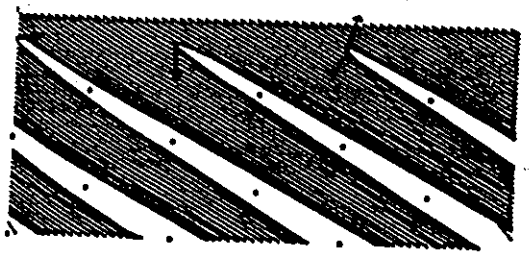

FIGURE #3 Collection of computer-generated trajectories for an ion beam incident on an ideal crystal along a low-index direction (taken from [8]).

scattering yield so that there is a minimum in the angular distribution of scattered ions at this aligned direction. At grazing incidence angle, for energies of a few keV or less the shadow cone angle may be greater than the incidence angle. Then all the atoms on the surface in an aligned row are hidden by their neighbours and a deep minimum, ideally zero, is produced.

One factor which tends to render the shadowing imperfect is the vibrational (thermal) motion. This effect is more pronounced at higher primary beam energies where the shadow cones are only a few degrees wide but at a few keV energies vibrational motion is a small correction since the shadow cones are usually much larger than the vibrational displacement.

The shadow cone can be obtained by calculating the trajectories for many different impact parameters (P) and determining the envelope of the innermost trajectories, since different trajectories touch the envelope in different regions of the shadow edge. The actual shape of the shadow cone depends on the interatomic potential, the energy of the projectile and the masses of the colliding particles. Several papers have been written which compare the different interatomic potentials [9,10] and it has become generally accepted that the Moliere potential describes quite well the interaction between an energetic ion and an atom in the solid.

$$V(r) = \frac{Z_1 Z_2 e^2}{r} \sum_{i=1}^{3} \alpha_i \exp\left(-\beta_i r/a\right)$$

where $\{\alpha_i\} = \{0.1, 0.55, 0.35\}$, $\{\beta_i\} = \{6.0, 1.2, 0.3\}$ and

$$a = \left(\frac{3\pi}{8\sqrt{2}}\right)^{2/3} \frac{a_0}{\left(Z_1^{2/3} + Z_2^{2/3}\right)^{1/2}}$$

is the Thomas Fermi length expressed in terms of the Bohr radius (a_0).

Standard classical two-body interaction theory can then be used to predict the shadow cone angle dependence on the primary ion energy and on both masses involved in the collision [11]. Table 1 shows several values of cone angles (θ) at a distance L = 5 Å from the silicon target atom using several different masses as incident particles. The projectiles (of mass M_1) used in the calculations were oxygen, argon, krypton and xenon, all of which had the same kinetic energy (5 keV).

Table 1 Typical shadow cone values

M_1 (a.m.u.)	P (Å)	R (Å)	$\theta=\tan^{-1}(R/L)$ [in degrees]
16.0	0.750	1.055	11.92
40.0	1.073	1.279	14.35
82.9	1.425	1.410	15.75
131.3	1.650	1.456	16.24

As stated earlier, certain incident shadowing directions will cause a decrease in the scattered intensity (e.g. channeling). This decreased intensity is not only expected for certain directions of incidence, but also for certain directions of ejection. This shadowing effect is then described as blocking. The

most prominent minima occur in directions where there is simultaneous channeling and blocking. This geometry is referred to as double alignment. The size of the blocking cone can be derived from the size of the shadow cone for a parallel beam by reversing the trajectory of the primary particle.

2.3 Charge exchange

The study of charge exchange between projectile atoms and a clean surface is of fundamental interest, both from a theoretical and an experimental point of view. Using LEIS we can examine the charge change that occurs during the single violent collision of the ion with one atom at the surface. The theory predicts very well the observed dependence of the charge fraction on the energy states of the electron in the ion and in the surface [12,13]. Due to the atom-surface interaction, electrons can be transferred from the ion to the target atom or vice versa. The quantity of interest is the charge state of the ion after the scattering event has taken place. The reflected particles are usually found in various excited states of the species but the usual experimental methods do not identify these.

Electronic transitions in which an ion near a surface atom could conceivably become involved are of the resonance, Auger and radiative types. However Shekhter [14] has shown that the probability of neutralization of an ion near a metal accompanied by radiation is very low (about 5×10^{-7}). The probability of any radiative process is expected to be low because the lifetime for radiation (about 10^{-8} sec) is very long compared to the time which even a thermal particle spends within a few angstrom units of the surface (of the order of 10^{-15} sec considering an oxygen ion in the low-keV region). Thus charge exchange to or from the incoming ion can occur through either an Auger (non-resonant) process or a resonant tunnelling process. Here it will be assumed that resonant

tunnelling is the dominant charge exchange mechanism because we consider only the conduction band of the target material and one energy level of the projectile atom. Deeper levels are tightly bound and cannot be excited because the motion of the atom and therefore the time-dependent perturbations acting on the electrons are too slow. For the same reason, no electrons can be excited into higher states, in particuliar into the electronic continuum above the vacuum level. Two-electron processes, such as the Auger process are much less probable than resonant tunnelling in cases where the latter is possible.

Resonant electron exchange between a moving ion and a surface atom occurs when the binding energy of the transferred electron is not too different. This mechanism of charge transfer is a pure one-electron process, which involves the transition of a single electron from or to the atom.

The general approach in describing this process is based on a solution of the Anderson-Newns Hamiltonian. For simplicity, it is assumed that this process takes place in a single nondegenerate atomic state which lies energetically within the target atom conduction band, and for this atom, a free-electron description is assumed to be valid. Also the projectile atom's kinetic energy is assumed to be in the intermediate range (keV) and the atom-surface interaction is treated in a first-order rearrangement approach, as was proposed by Gadzuk [15] for the description of the chemisorption of alkali atoms on a metal surface.

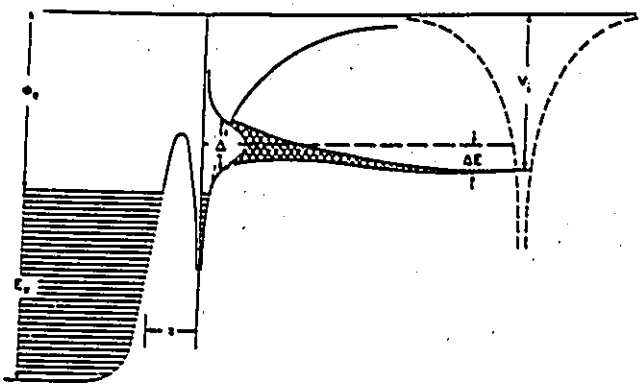

FIGURE #4 Energy level diagram for the interaction of an alkali atom with a metal surface (taken from [12]).

The unfilled electron states of the target atom are described by free waves inside a potential box with a total energy equal to the sum of the work function and the Fermi energy. Note that outside the box, the wave functions decay exponentially. When the projectile ion is brought close to the surface atom its originally sharp *ns* valence level shifts and broadens into a band of finite width. Note that *n* is an integer which refers to a particuliar s-type orbital. This shifting and broadening of the valence level is illustrated in FIGURE #4.

The origin of the level shift (ΔE) can be understood with classical electrostatic theory. Basically the level shift is due to the interaction with image charges, induced in the surface. Compared to the situation at infinite atom-surface distance, the valence electron experiences an extra repulsion from the image of the core and extra attraction of its own mirror charge. To first order the level shift is determined by the classical image potential where z is the atom-surface distance and k^{-1} takes into account the finite screening length of the target atom.

$$\Delta E = \frac{1}{4\ (z + k^{-1})}$$

The level width (Δ) is caused by the overlap of the incoming ion and target atom wave functions. This overlap makes resonant electron tunneling through the potential barrier between the ion and the atom possible. Simply stated, the probability for a resonant transition of the valence electron to an unoccupied target state determines the lifetime of the electron near the

atomic core. This finite lifetime relates via Heisenberg's uncertainty relation to the level width. To first order, the level width is given by Fermi's golden rule where the sum has to be taken over all metal states $|k\rangle$ degenerate with the atomic $|a\rangle$. The symbol ρ denotes the density of the metal states, which varies within the free-electron model as $\varepsilon^{1/2}_k$. V is the unperturbed interaction of the valence electron with the ion core. To a good approximation, the level width is an exponentially decaying function of the atom-surface distance z.

$$\Delta(z) = 2\pi \sum \rho(\varepsilon_a) |\langle a|V|k\rangle|^2$$

This perturbation-theoretical description of the interaction between an ion and a surface atom is useful if the width Δ of the atomic state is small with respect to the width of the conduction band. In this case perturbation theory provides a picture of a relatively localized atomic state, perturbed by the presence of the target atom.

Several calculation techniques have been developed which give generally good agreement with experimental measurements. A property of these models is that the collision process is effectively divided into three parts: the initial interaction before the primary ion actually reaches the target atom, the hard (binary) collision and finally the outgoing interaction between the two particles. Experimentally only the initial and final charge state of the primary ion are measurable, the intermediate part is not directly accessible.

Since the mid 1960's, it has become generally accepted

that the first two parts of the interaction do not contribute in determining the final charge state. It has been generally assumed in many theories that the scattering properties are independent of the initial charge state, and some of the formulations support this assumption. The vast majority of experiments use positive ion beams because these are the easiest to produce and are most readily available, so that this assumption, although accepted for many years, has not been experimentally verified until now. The theory of nearly resonant charge exchange was examined in detail and good agreement was found with the measurements [16]. In spite of this good agreement, none of these experiments distinguished between neutralization on the way in or on the way out. Bronkers and de Wit [17] compared Ne^+ and O^- (from fragmented H_2O^-) scattering and concluded that the charge state before the hard collision was unimportant and that the final charge state is determined during the outgoing trajectory.

We report a more direct experimental test of the loss of memory of the initial charge state during ion surface scattering. Measurements of the ratio of negative to positive ions scattered using the same primary ion beam (mass and energy) but first of positive ions and then negative ions. If the collision process is independent of the initial charge state, then all the outgoing properties of the interaction should be identical.

CHAPTER 3 - Experimental apparatus

3.1 Requirements

In order to do Low Energy Ion Scattering (LEIS) measurements, it is necessary to have a system which contains the following components:

1) Ultra-high vacuum (UHV) environment for the sample. (see Appendix I)

2) An ion source and accelerator to produce an ion beam with a narrow and well defined energy and angular spread.

3) A beam line with mass selection capabilities

4) A manipulator with translational/rotational movement of the sample holder so as to position and orient the target with regard to the beam.

5) Facilities for producing a clean surface. This usually requires target heating and ion sputtering systems.

6) A detector for the ejected particles which has angular and energy resolution and which can be rotated around the target for angular distribution measurements.

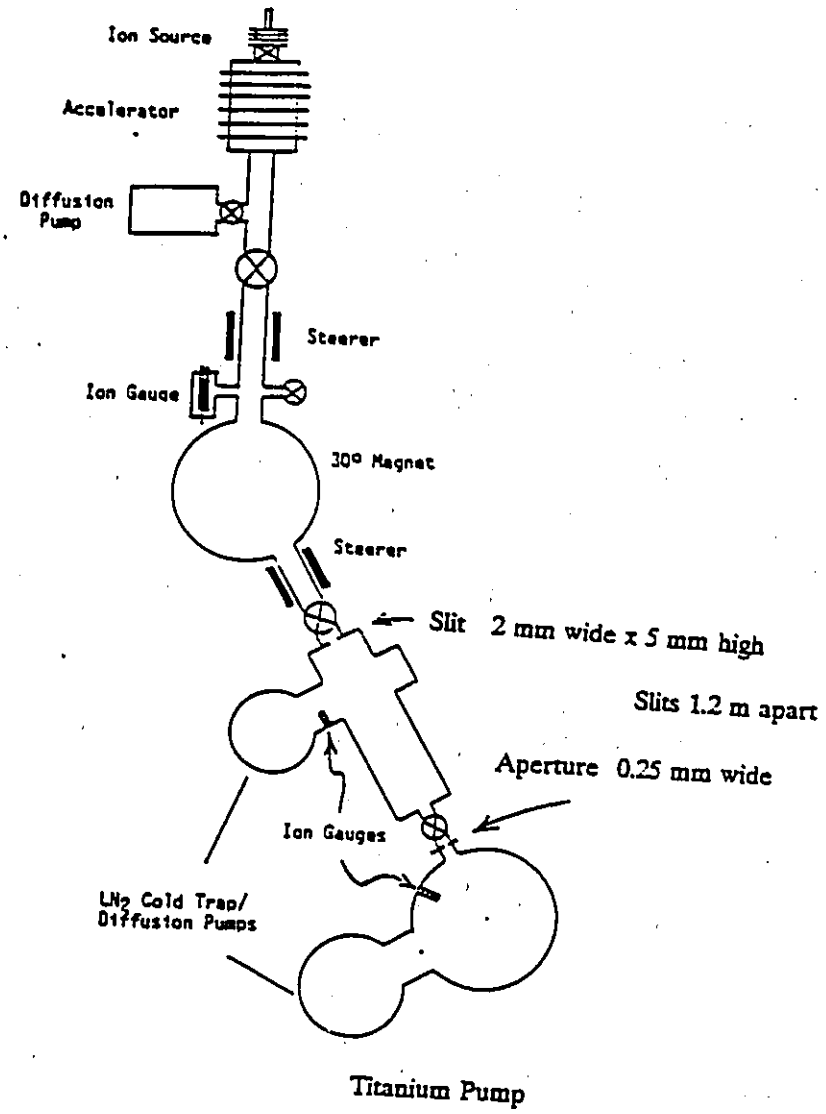

FIGURE #5 Schematic overview of the experimental apparatus.

3.2 Ion production

The ions we use are produced by a radio-frequency (RF) ion source. This type of ion source produces charged particles (in the keV range) in fluxes of the order of microamps (μA). Additionally it provides the option of creating both positive and negative ion beams. Other types of ion source are available which avoid the main restriction of the RF source which is that the element must be in the gaseous form. However these are less reliable, or have short maintenance intervals or produce very low intensity beams. They almost always use thermionically emitted electrons from a hot filament to ionise the atoms, so that negative ion extraction is not possible because of the large electron background.

The discharge is produced inside a glass tube by external electrodes coupled to a high frequency oscillator. The radio-frequency waves excite the gaseous atoms or molecules by creating a strong electro-magnetic disturbance. Sufficient RF power is required to fill most of the volume with plasma. A positive anode, in this case a wire, is sealed into the glass tube and since the plasma is basically a conductor, the whole of the discharge is considered to be at this same potential (typically 1 kV). The only other conducting surface exposed to the plasma discharge is an axial-tube electrode, usually called the exit canal. The ionized atoms are extracted from the positively biased plasma boundary and subsequently accelerated towards the canal (HV_1) where some escape into a much lower pressure region. Inside the tube the ions are in

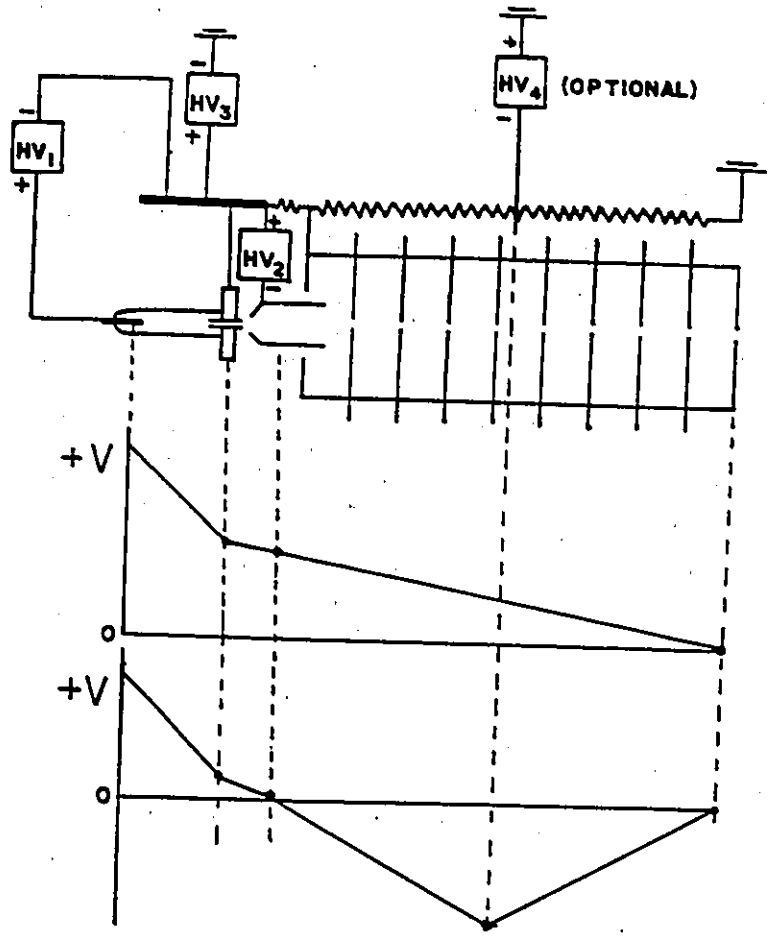

FIGURE #6 Ion source potential distribution. Note that the two voltage graphs represent qualitatively the potentials to which the ions are subjected to while passing through the ion source.

a nearly field-free region before emerging into the roughly uniform electric field of the accelerator column (the top voltage graph of FIGURE #6).

The fringe field between these two regions behaves as an ion optics lens. HV_2 provides focussing so that the beam can be converged to a small width beyond the accelerator. The energy of the ions is determined by the potential change between the plasma and ground and is approximated by the sum of the anode potential (HV_1) and the accelerator voltage (HV_3), minus a small voltage used for the ionisation of the gas in the glass tube. The anode potential can range from 0 kV to 2.5 kV but for about 2 kV and over the plasma discharge tends to be unstable and this disturbance reduces the stability of the ion beam. The accelerator voltage can range from 0 kV to 150 kV.

To invert the beam polarity all the electric fields are reversed except in the ion source itself. The negative ions are produced from positive ions inside the exit canal by electron capture collisions with the residual gas present there. This negative beam required somewhat different operating conditions and the ion flux was approximately a few percent of the typical positive ion beam current. Interestingly, the energy of the extracted ions was found to be determined only by the accelerating voltage. This polarity reversal option is a distinct advantage which is not available to many research groups presently engaged in this field of research.

Certain measurements required a low energy beam and using

the present voltage distribution did not produce sufficient ion current. By applying a negative high voltage (HV_4) partway along the resistor chain (on the accelerator column), the ion flux was greatly enhanced. This ion production enhancement can be explained as follows; the plasma extracted at an initial energy is accelerated to a high potential which allows a higher extraction efficiency of the ions from the plasma boundary. The ions are then decelerated back to there initial energy (lower voltage graph of FIGURE #6). As a result, low energy ion beam current was increased by a factor of about 30.

3.3 Mass selection and beam collimation

The ion beam is deflected by a 30° bending magnet through two narrow slits. The magnet separates out different ion masses by deflecting each mass at a different radius of curvature (FIGURE #7). A simple relation can be obtained by considering the forces involved for a uniform magnetic field perpendicular to the velocity:

$$\frac{m\,v^2}{r} = q\,v\,B$$

where m, q and v are respectively the ion mass, electric charge and velocity, B is the magnetic field and r the radius of curvature. The velocity can be expressed as a function of the accelerating potential V.

$$E = q\,V = \frac{m\,v^2}{2}$$

thus

$$v = \left(\frac{2\,q\,V}{m}\right)^{1/2}$$

Combining the first and third equations and rearranging we obtain

$$\frac{m\,V}{q} = \frac{r^2\,B^2}{2}$$

In the right side r^2 is a geometrical constant for all ions which pass through the collimating apertures of the system. All ion mass/charge ratios should therefore lie on the same straight line of a graph of m V / q as a function of B^2 (FIGURE #8).

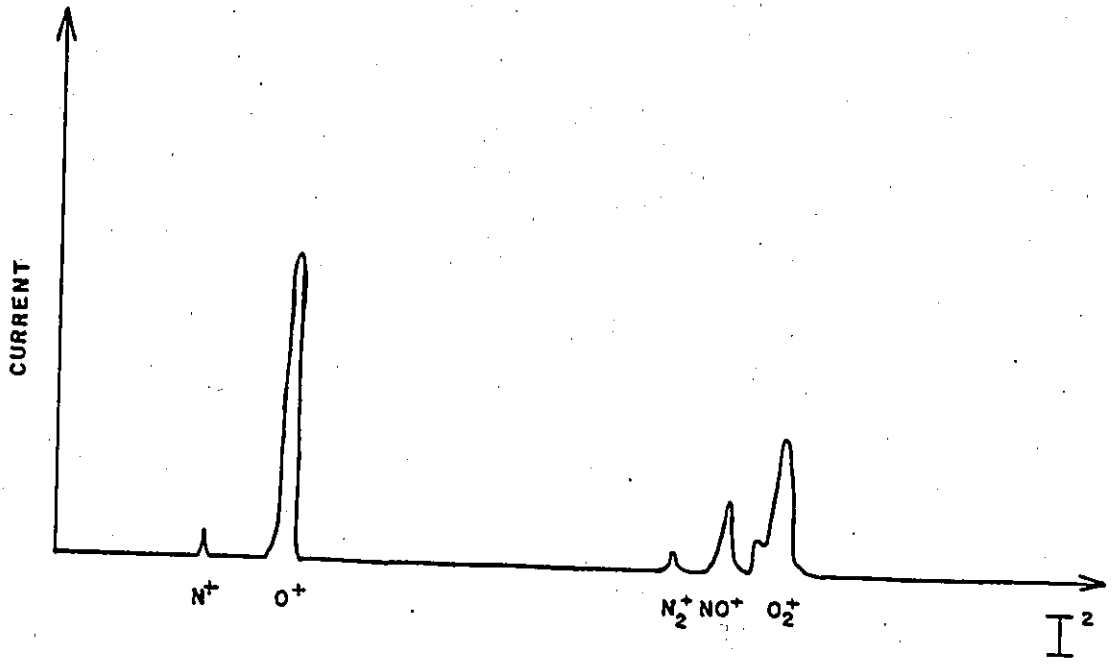

FIGURE #7 Mass spectrum of the ion source. The ordinate represents the current to ground measured on the entrance slit of the main chamber (slit #2) while the abscissa is simply the square of the current (I) sent through the beam bending magnet (as stated in the text I is proportional to the magnetic field B).

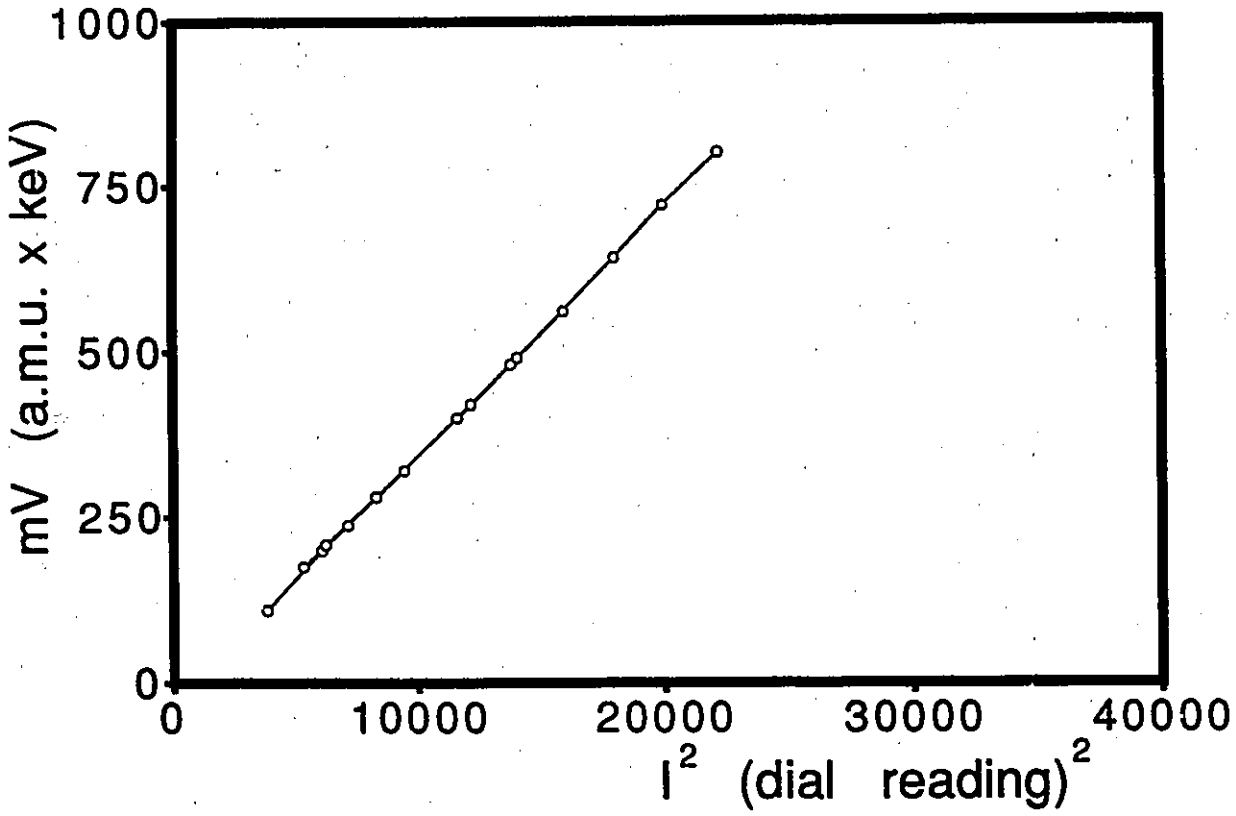

FIGURE #8 Mass calibration graph

The straight line seen on the mass calibration graph was obtained using a well known ion mass (i.e. high purity oxygen in the ion source) for many different accelerating potentials. The other atomic or molecular ions can be determined by interpolation. In practice, the current I through the magnet can be used as a measure of B and the hysteresis effects are kept small by always scanning in the same direction.

The ion beam is collimated through the system by the help of adjustable weak transverse magnetic fields perpendicular to the beam line. These "steerers" consist of four coils, wound around a square iron core, surrounding the vacuum pipe through which the ions travel. The coils on opposite sides are connected in series so that their fields are opposed inside the iron. The return fields emerge from the iron and produce a weak, nearly uniform field in the vacuum (Figure #9). Magnetic fields of a few hundred gauss over a 20 cm path are sufficient to deflect the ion beam by a few degrees. Since the fields are small, there is little iron saturation and the current/field relation is nearly linear. Consequently a change in the left/right deflection, which is produced by a change in the magnitude of the current in the coils on each side (vertical field), does not disturb the up/down deflection which is produced by the top and bottom coils (horizontal field). Therefore they act effectively as independent controls.

These magnetic steerers used in conjunction with an optimum focus potential produced an O^+ ion beam of a few nanoamps

(nA) on target. The tight geometry of the ion beam was defined by two slits set about 1.2 meters apart. The first slit was 2 mm wide by 5 mm high and the second was only 0.25 mm wide. This geometry produced a collimated beam that had a narrow energy spread and its angular spread (in the horizontal axis) was about 2 mrad. Note that the ion currents were measured with a Keithley picoammeter electrically connected to the sample in the main chamber, and no correction was applied for secondary electron emission.

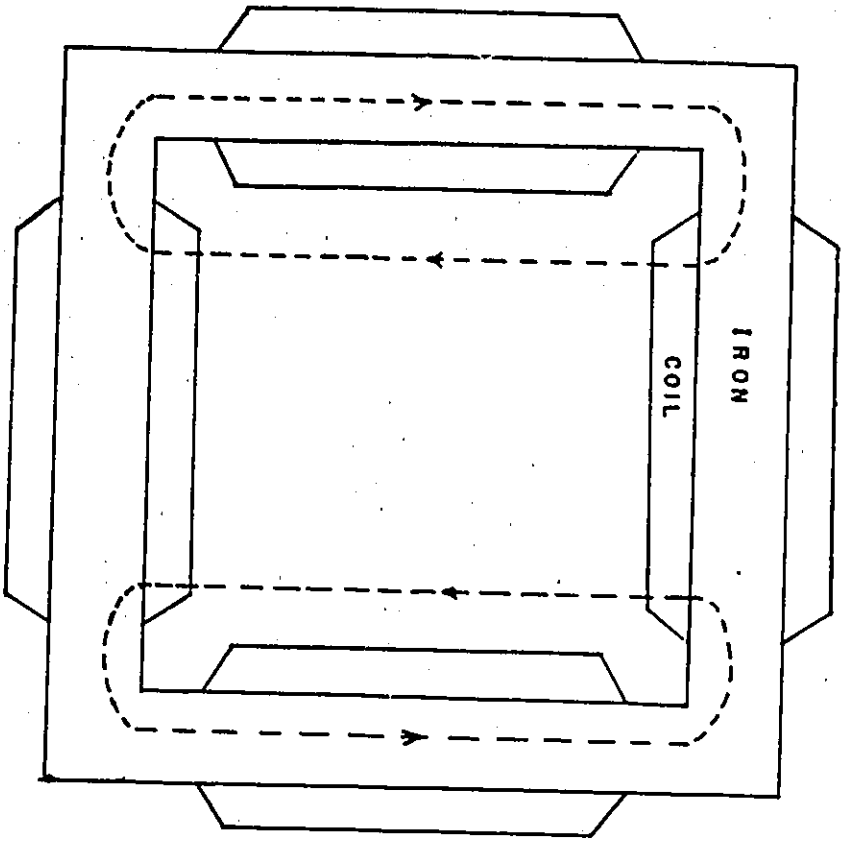

FIGURE #9 Schematic of the magnetic steerers. Note that the dotted lines represent the magnetic field lines produced by the top and bottom coils.

3.4 Sample holder

The steady and narrow ion beam hit a target surface (Si(100) wafer mirror-polished) at the centre of main chamber which was firmly held by molybdenum (Mo) clamps to a Mo holder-plate. The sample holder was attached to a high precision manipulator with X, Y and Z translational movement, rotation about a vertical axis and also rotation in a plane perpendicular to the target normal (Figure #10 a)). The system therefore had five degrees of freedom to accurately position the sample surface.

These sample movements were most easily accomplished when the vertical axis of rotation (the Z axis) was at the surface; with off-axis samples it was more difficult to make the Z axis rotations and at the same time maintain the sample position. The translational resolution of the manipulator was 0.005 mm for all 3 axes. The angular resolution was 0.1° on the primary rotation axis and 0.3° on the secondary axis.

The manipulator was equipped with an electron beam heating accessory (FIGURE # 10 b)). This type of heating was provided by an electron emission filament (thoriated tungsten) located directly behind the sample backplate which also acted as a grounded anode. Some thermal radiation heating was produced but this was significantly increased by applying a high negative voltage to the filament to produce about 25 Watts of electron power. This type of heating allowed temperatures as high as 1200°C to be reached very easily.

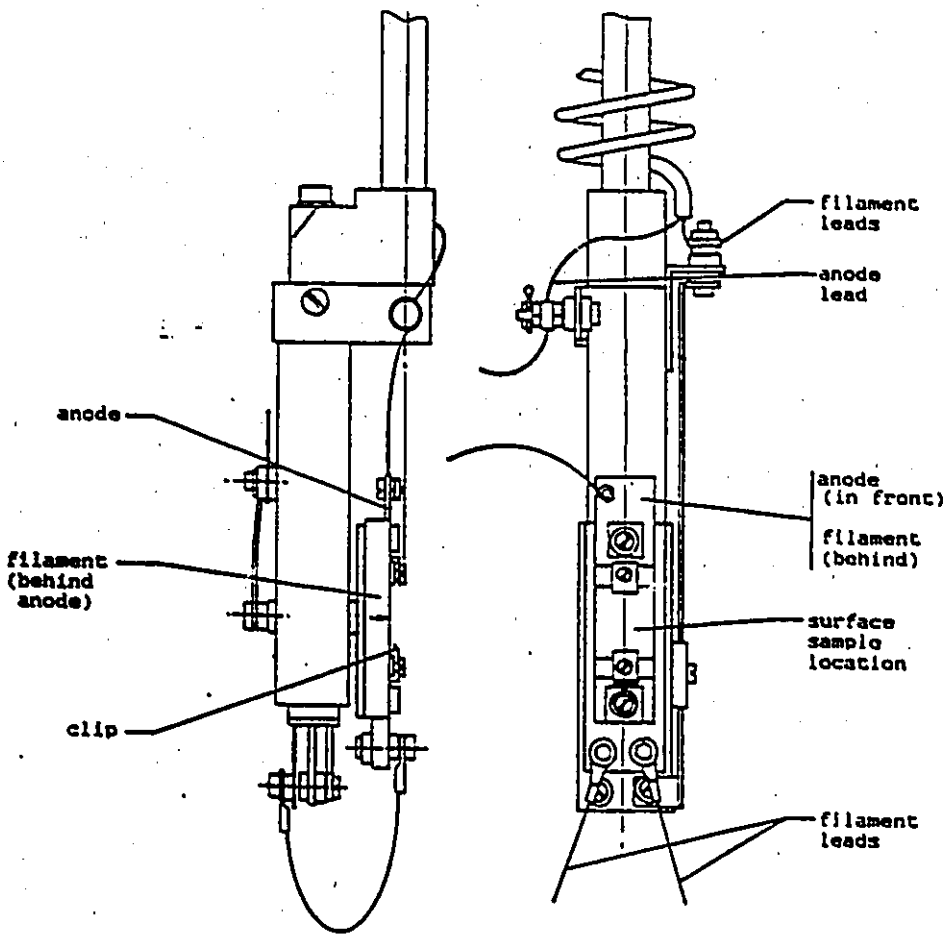

FIGURE #10 a) Electron beam heater mounted on a two rotation axes sample holder.

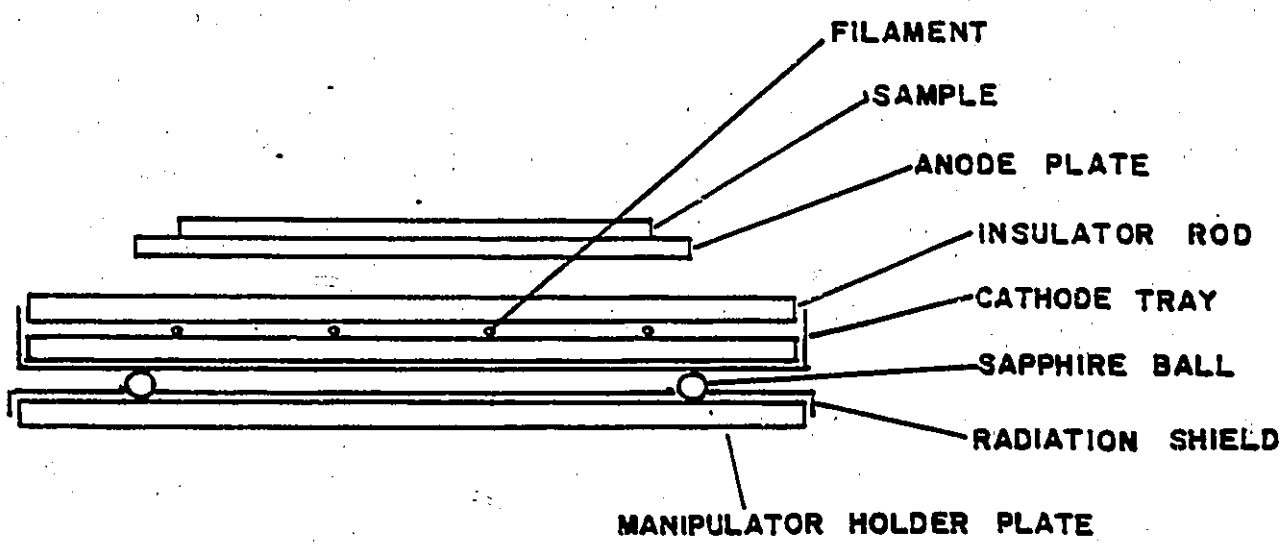

FIGURE #10 b) Electron beam heater schematic (top view)

The temperature of the sample surface could be monitored by means of one or two NiCr/NiAl thermocouples which can be affixed to the sample surface or directly upon the Mo backplate. Note that the negative potential filament produced stray electrons some of which escaped into the chamber where they struck the stainless steel walls and caused surface electro-desorption (primarily hydrogen). This surface outgassing during heating was unacceptable because the pressure rose by a factor 10 at least. The solution was to operate the electron emission filament at ground potential and have the anode positively biased. The stray electrons were then no longer attracted to the chamber walls since they were at the same potential. Unfortunately this arrangement prohibited the use of thermocouples in contact with the backplate (thermocouples operate only near grounded surfaces).

3.5 Energy analyser

Following the ion-atom collision, the scattered and recoiled ions were energy analysed. The plane of scattering was horizontal, with the incident angle being determined by the vertical rotation axis of the manipulator and the scattered angle by the position of the detector on the horizontal racetrack (Figure #11). Most measurements of this type are accomplished using either an electrostatic or magnetic analyser. Since electrostatic analysers (ESA) are considerably simpler to build and operate then magnetic ones, they are by far the most popular, and this type was chosen for the present system.

There are many different types of electrostatic analysers and their focussing properties have been well discussed by several authors. Two of the most common designs are the 180° and the $\pi/\sqrt{2}$ (or 127°) electrostatic analysers. The former basically consists of two concentric hemispheres: a particle beam enters through an aperture into the space between the two electrodes and is focused to another aperture, directly opposite after a 180° deflection. The main advantage of this type of analyser is that the focussing is in two dimensions; the disadvantage lies in the difficulty involved in accurately machining and constructing the device.

The 127° analyser consists of two cylindrical concentric curved plates separated by a small gap, with entrance and exit slits at an angle of 127°. It has been shown that focussing with good resolution occurs for a deflection of 127° 17′ [18]. This

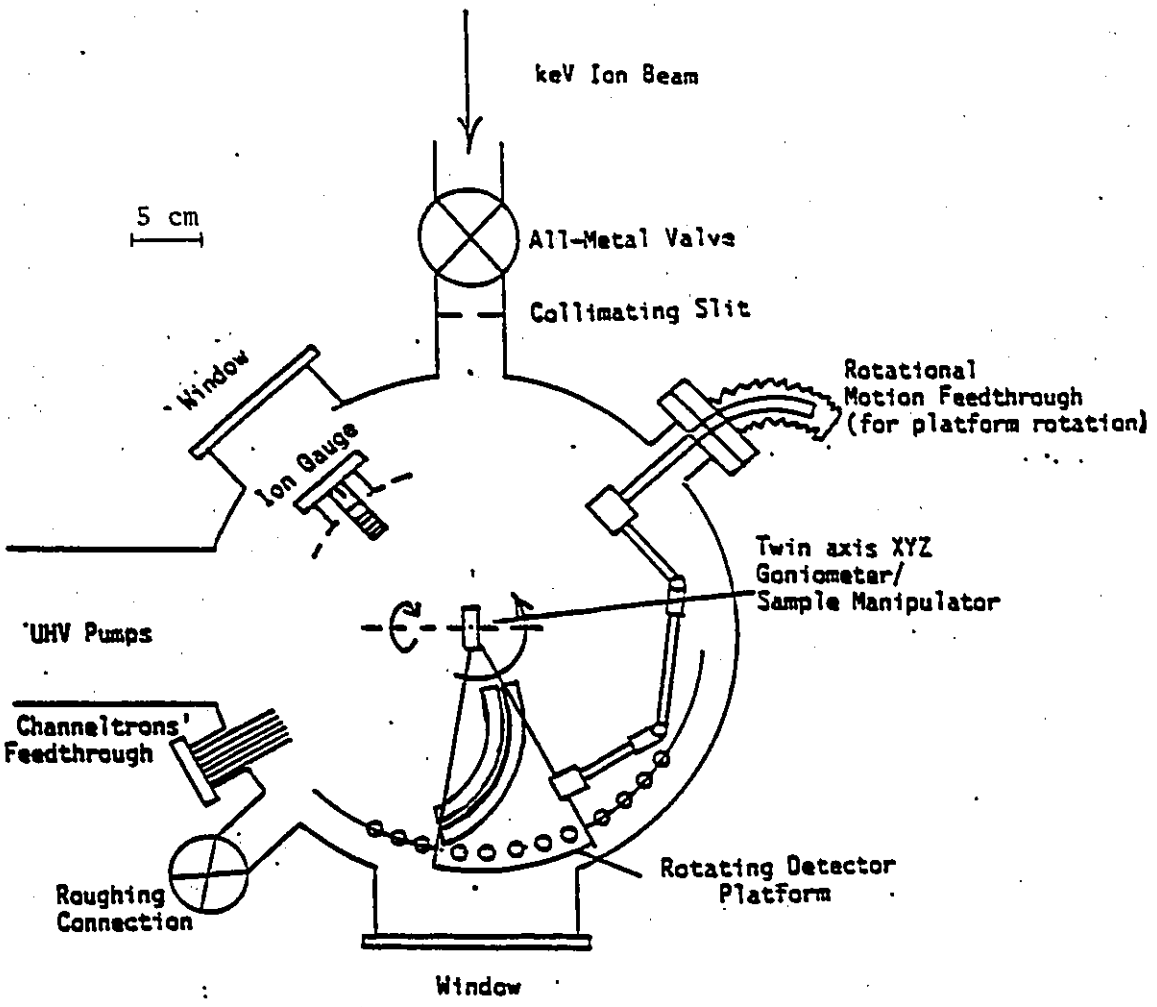

FIGURE #11 Main chamber schematic overview

analyser is single focussing, since the field is everywhere horizontal; there are no vertical forces and therefore no vertical focussing. Appendix II gives the first order analysis of the ion optics of this system.

The energy resolution is simply given by the following equation:

$$\Delta E/E = (\text{width of slit \#2} + \text{width of exit slit}) / r_o$$

With the size of the beam and exit apertures (0,25mm wide x 7mm high and 0,5mm wide for slit #2 and the exit slit respectively), the theoretical resolution is 1.3%. A convenient test of the analyser was to run the ion beam directly into the ESA (Figure #12). Note that the beam intensity had to be reduced by a factor of about 1000 to avoid damaging the detector. The beam energy resolution from the magnetic deflection analyser was much better than that of the ESA so that the beam for this test was effectively monoenergetic.

This type of ESA has the practical advantages of a simple design which makes construction and alignment less critical, while still offering good energy resolution. It must also be constructed entirely from UHV compatible materials such as good quality aluminum and stainless steel for the frame and electrodes. The insulation for the electrodes is provided by teflon material, but we can also use certain ceramics and machinable glass which are UHV compatible.

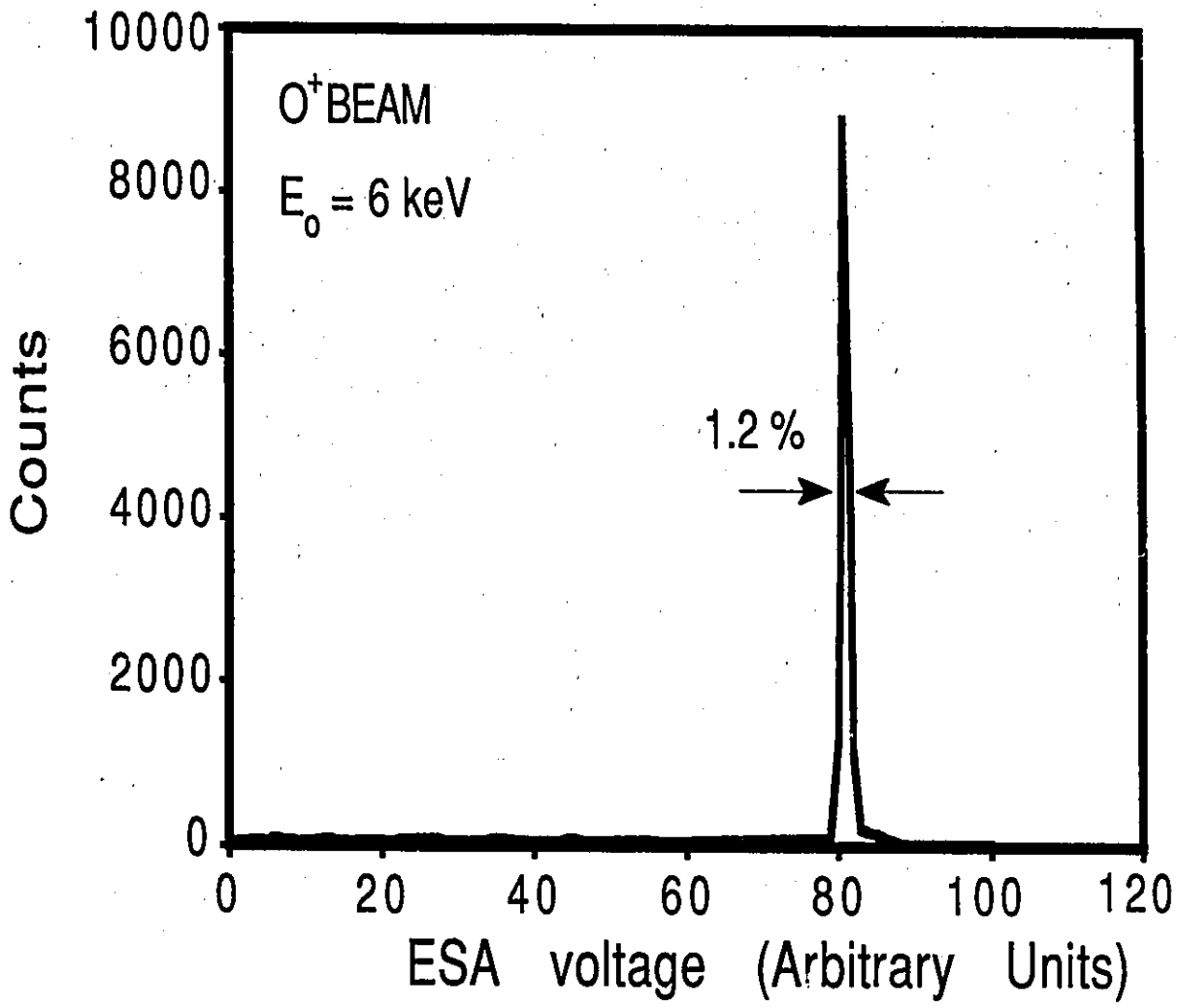

FIGURE #12 Energy spectrum obtained by running an O^+ beam of 6 keV directly into the ESA.

3.6 Detectors

The energy selection was accomplished by the ESA but the actual particles were counted individually with the aid of a channel electron multiplier (CEM) mounted behind a small slit (0.5mm wide). The detection efficiency of CEM for ions has been shown to be independant of energy in the range of 2 to 10 keV [10]. Below 2 keV the sensitivity is lower because the secondary emission coefficient decreases so that the probability that one of the several secondary electrons emitted from the entrance cone following the initial ion impact will be captured and multiplied is less. Above 10 keV the sensitivity is also lower but for a different reason. The ions, possessing more kinetic energy, have a longer range in solids so that again there is a decreased probability of a secondary electron from the initial impact being captured and subsequently multiplied.

When the ion beam entered the UHV chamber there was an abundance of secondary electrons emitted throughout the chamber. These stray electrons were unacceptable since the CEM counted these low energy electrons as ions. Interestingly enough, the maximum energy of these electrons can be evaluated from the simple kinematic equation stated earlier for a recoil particle. The maximum energy such an electron can possess following a head-on collision is given by the following equation where E_0 is the kinetic energy of the incoming ion and m_1 and m_2 are the masses of the projectile and the electron respectively. The right side of the equation is for the case of an oxygen ion colliding with a target

electron (mass of oxygen atom is about 1837 times the mass of the electron).

$$(E_r)_{max} = \left(\frac{4\, m_1\, m_2}{(m_1 + m_2)^2}\right) E_0 = \frac{4 \times E_0}{1837}$$

This electron problem was resolved by negatively biasing the front cone of the CEM sufficiently to completely repel all the stray electrons from ion scattering. However the negative electrode of the ESA itself was a source of electrons from field emission, and for a sufficiently high operating voltage (on the negative electrode), the stray electrons were again a problem. By increasing the negative bias to the CEM front cone (to about 1 to 2 keV), these higher energy electrons were also repelled.

In addition to the CEM behind the ESA, there was also a second CEM located in the UHV chamber in direct line of sight of the sample. Its sole purpose was to monitor the actual ion intensity on the target during measurements. This method took into account beam fluctuations and in certain cases it allowed us to normalise our measurements. This method of ion counting was preferable to measuring the current on the target (since a Faraday cup was not used) because it avoided problems of secondary electron emission effects that occured during sample heating, which gave quite false ion current readings.

It is important to note that the wiring for both CEM's was initially a problem because of the limited number of materials which are UHV compatible. Bare copper wires (Cu is a UHV material) proved to be unsatisfactory because of the electrostatic pick-up

between the CEMs involved in having unshielded wires. This problem was solved with teflon coaxial cable (with the outer insulation removed). The digital output signals from the two CEM's were changed to low impedance by preamplifiers just outside the vacuum and then sent through coaxial cables to the electronic system where they were amplified and displayed on scalers. These pulses were also fed into a computer for data reduction and storage.

3.7 Reflection high energy electron diffraction (RHEED)

In addition to the ion scattering equipment, the chamber contained an electron diffraction device which enabled us to examine the surface in another way. RHEED is a technique for surface structure analysis; electrons which are incident upon a flat surface at grazing angle produce a diffraction pattern characteristic of the atomic surface arrangement. Since the normal component of the incident electron momentum is small, the penetration of the electron beam is also small and consequently the information we obtain is from the first few atomic layers of the surface and not the bulk. The electron gun was directed horizontally on an axis perpendicular to the beam and the RHEED pattern was observed on a fluorescent screen located directly opposite the electron gun (on the other side of the target).

This RHEED pattern was very useful for quickly examining the crystal structure of a surface and in some cases identifying the presence of impurities. However it was found that ion scattering was a more critical test for hydrogen and carbon build-up. This part of the research will not be described in detail because it is the subject of another thesis.

CHAPTER 4 - Sample preparation

As earlier stated the importance of a clean silicon sample for surface studies is fundamental for these measurements. Prior to inserting the Si(100) sample into the UHV system, it was treated with an oxidation process. We are grateful to the Microstructures Laboratory at NRC for both providing the samples and performing the oxidation. This process consisted in putting the silicon wafer in an oven while exposing it to an ozone gas for about an hour. It is estimated that an oxide layer of about 0.1 microns thick was produced in this way. As shown in FIGURE #13 a) this ozone layer completely hid the features in the energy spectrum except for the hydrogen recoil peak and it was easily removed by heating (temperature of about 850°C) since SiO has a higher vapour pressure than Si. This cleaning procedure was later found to produce a surface cleaness identical to that which was obtained by simply sputtering and annealing when a sputter gun was available. Note that FIGURE #13 a)b)c)d) are energy spectra of ions scattered at 35° to the silicon surface for 5° incident ion beam. The arrows show the predictions for an elastic collision with a single atom on the surface.

For repeated measurements, and after an overnight contamination from the residual gas, the target was recleaned by 2 keV argon ion sputtering (2 $\mu A/cm^2$), for 15 to 30 minutes depending on the contamination present. It was then heated sufficiently (approximately 700°C for 10 seconds) to outgas the surface argon or even higher (about 1000°C for 20 minutes) to anneal the crystal

structure. The first case produced an amorphised surface with a RHEED pattern that showed no diffraction spots. The ion scattering spectrum (FIGURE # 13 b)) showed a clean silicon surface peak but with no channeling effects at all. The second case, which required more intense heating, produced a clear Si(100) 2 x 1 RHEED pattern. This notation for describing a particuliar surface was suggested by Wood [19] and is now widely used in crystallography. Si(100) 2 x 1 signifies a clean (100) silicon surface with a diperiodic surface structure in which the periodicity is two unit cell widths in one direction and one unit cell width in the perpendiculiar direction. The energy spectrum from a sputtered and annealed sample (Figure #13 c)) taken in a non-crystalline direction was indistinguishable from the amorphised surface (Figure #13 b)) which is pretty much what one would expect. Note that following about 48 hours of exposure to the residual gas (2.5×10^{-10} torr), the energy spectrum (FIGURE # 13 d)) showed a growing oxygen contamination peak (oxygen beam/oxygen target atom). For a residual pressure of 2.5×10^{-10} torr, Langmuir's equation predicts that one monolayer of atoms will stick to the surface every 4000 seconds. Note that this value assumes a sticking probability of unity.

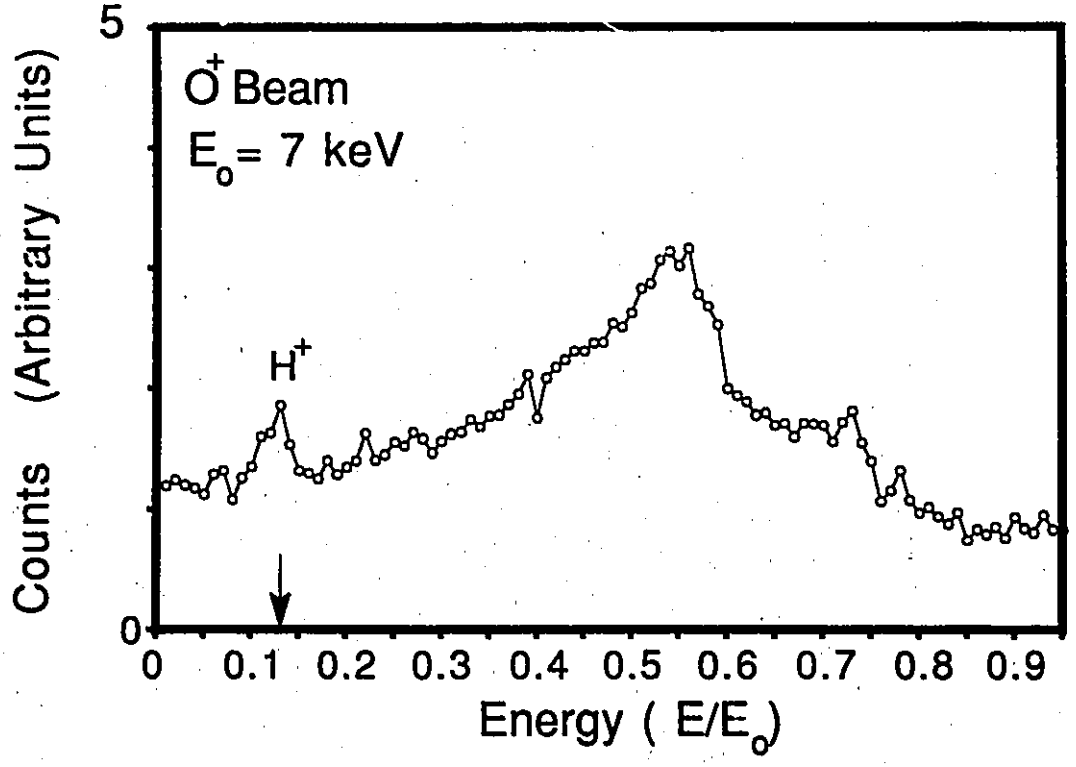

FIGURE #13 a) Ozonated sample (contaminated)

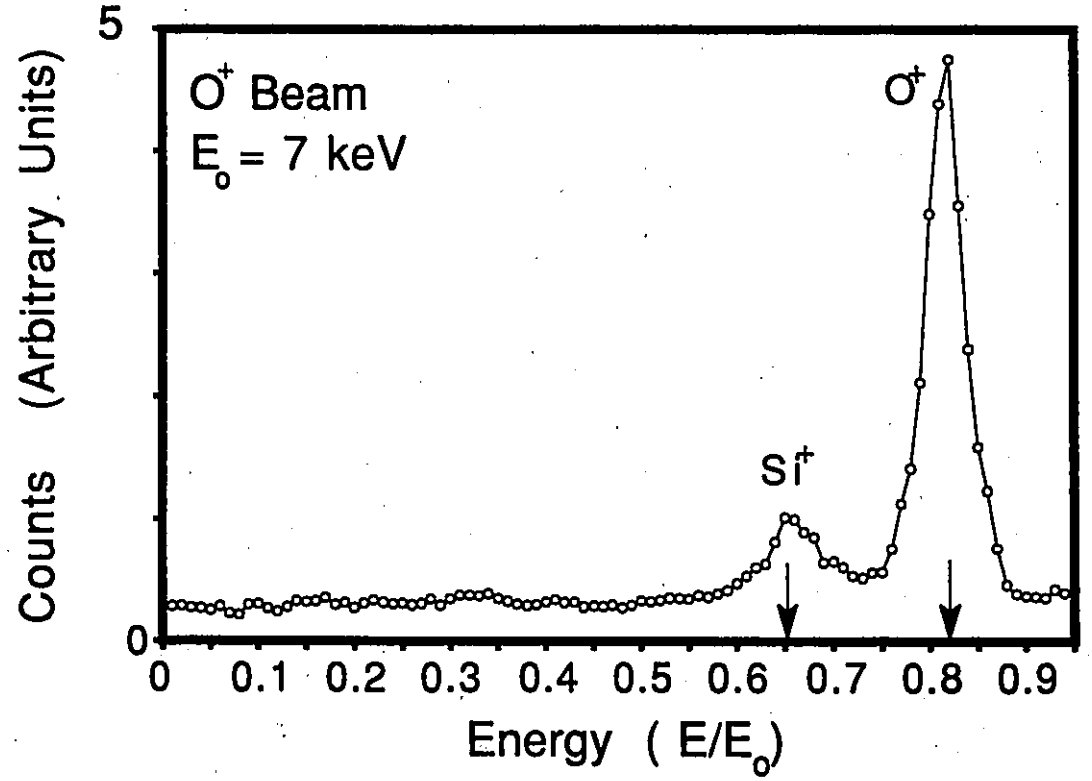

FIGURE #13 b) Sample sputtered

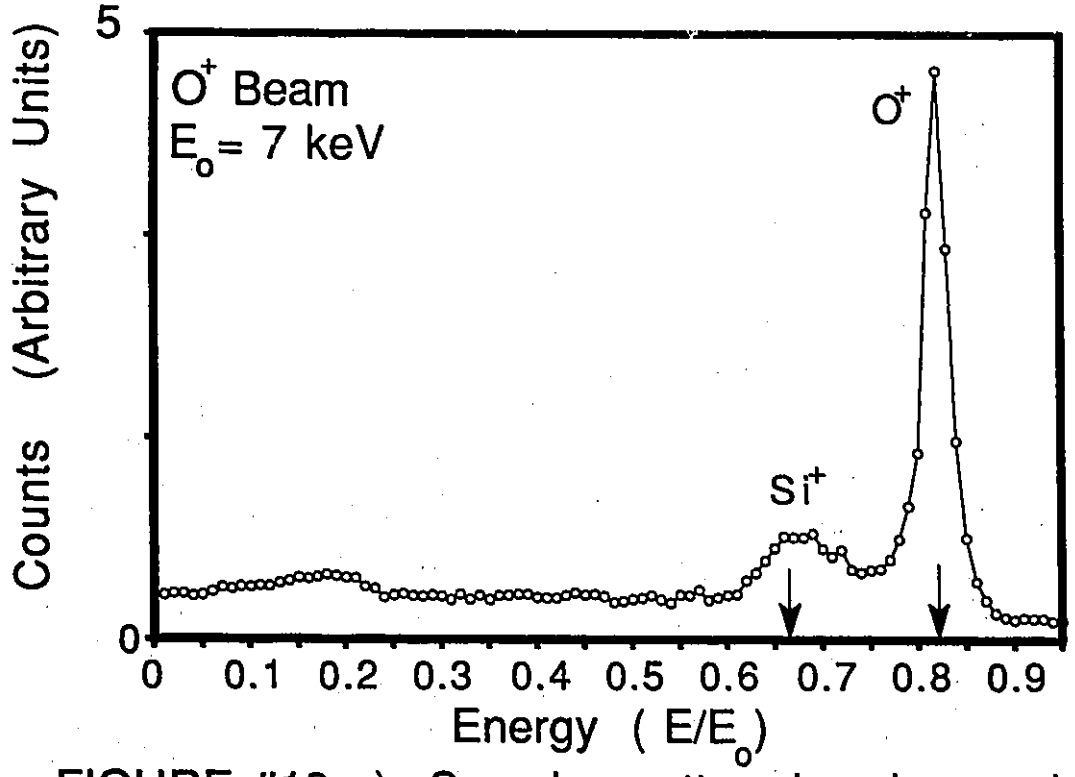

FIGURE #13 c) Sample sputtered and annealed

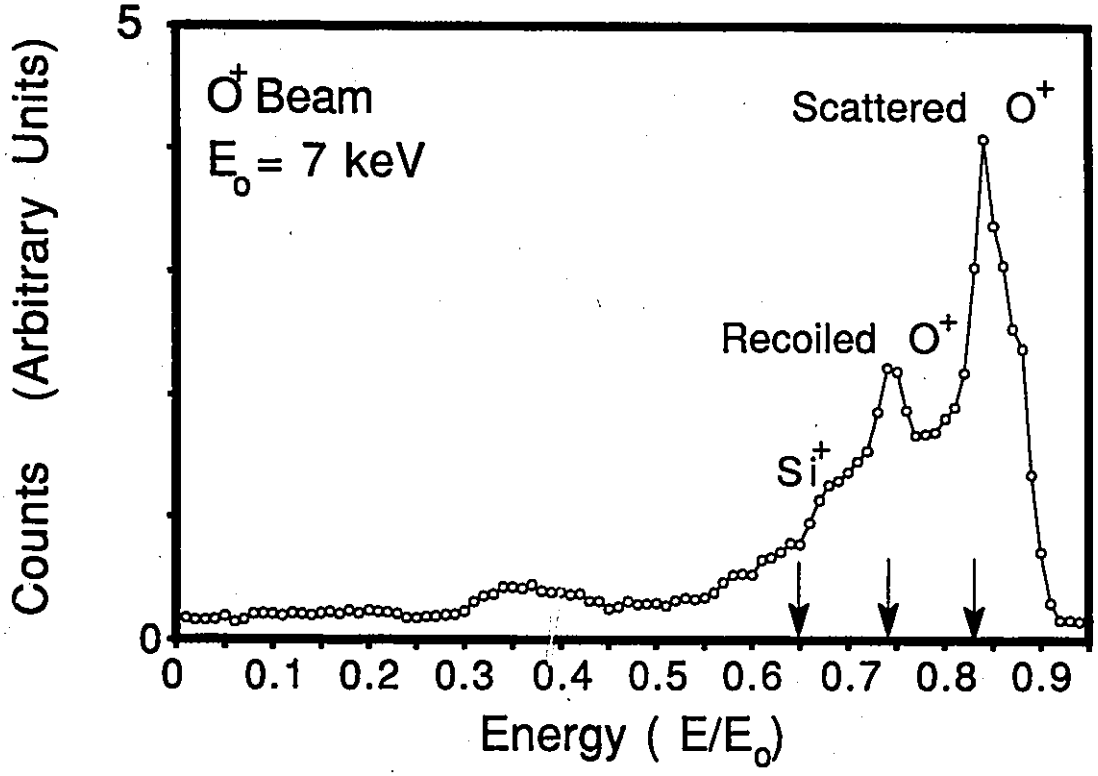

FIGURE #13 d) Sample contamination from residual gas

CHAPTER 5 - Experimental measurements

5.1 Channeling and blocking spectrum of Si(100)

Beginning with a clean Si(100) 2 x 1 single crystal surface (e.g. the previously described preparation procedures had been followed shortly before the measurements) and a 7 keV O^+ ion beam, the anisotropy of the scattered ions was measured. The O^+ primary ions arrived at 5° incidence and the measurements where taken at an outgoing angle of 35°. Note that this particuliar scattering geometry was chosen since calculations showed that a shadowing and blocking pattern would be observed.

FIGURE #14 shows the intensity variation of singly-scattered (SS) oxygen ions from silicon atoms as a function of azimuthal orientation (the sample was rotated about an axis perpendicular to the surface). The relative intensities where estimated from the peak areas of the energy spectrums.

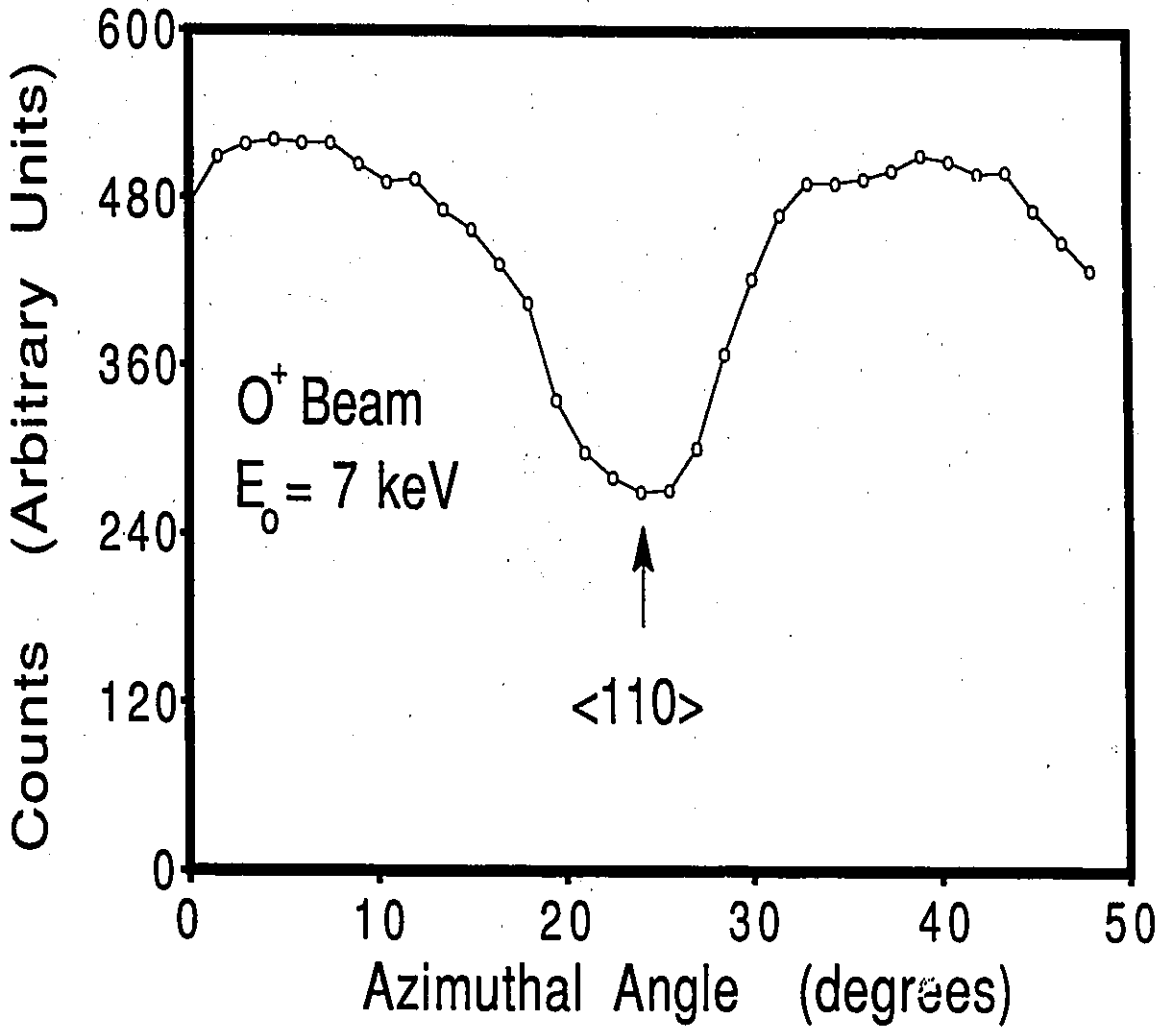

FIGURE #14 Surface channeling and blocking pattern for a clean Si (100) 2 x 1 crystal measured with 7 keV oxygen ions.

5.2 Charge dependence of ion surface scattering

This first part of the experiment was more a test for our newly built apparatus. The second part (it has been proposed for separate publication as a paper) was an experimental test that shows the loss of memory of the initial charge state during ion-atom surface scattering (FIGURE #15). The charged particles entered at 5° grazing angle (Ψ) and the detection system was set at 25° outgoing angle ($\theta - \Psi$). Note that this angle (θ) was chosen since it was large enough to kinematically separate out the Si recoil peak and small enough to allow a sufficient counting rate for the SS oxygen peak. Positive and negative oxygen ion beams of same energy were scattered from a clean, amorphized silicon surface for primary energies ranging from 6.8 keV to 19.0 keV.

Figure #16 shows energy spectrums using 6.8 keV and 16 keV primary oxygen beams. All the peaks appeared at the calculated energies (the arrows), confirming that they were mainly due to single atom surface scattering. Notice that the negative ions have a continuum below the surface peak whose area increases with increasing primary beam energy. This supports the observation of Bronkers and de Wit [17] that multiple subsurface scattering, which involves energy loss by inelastic processes, is more evident in the scattered negative ions than the positives.

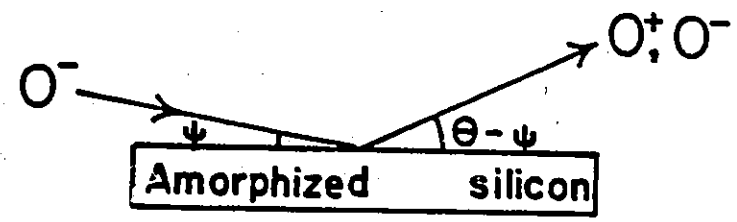

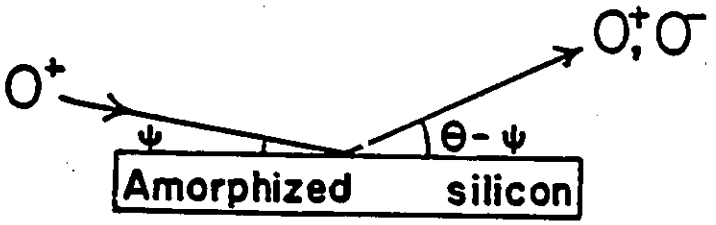

FIGURE #15 Diagram of the scattering geometry.

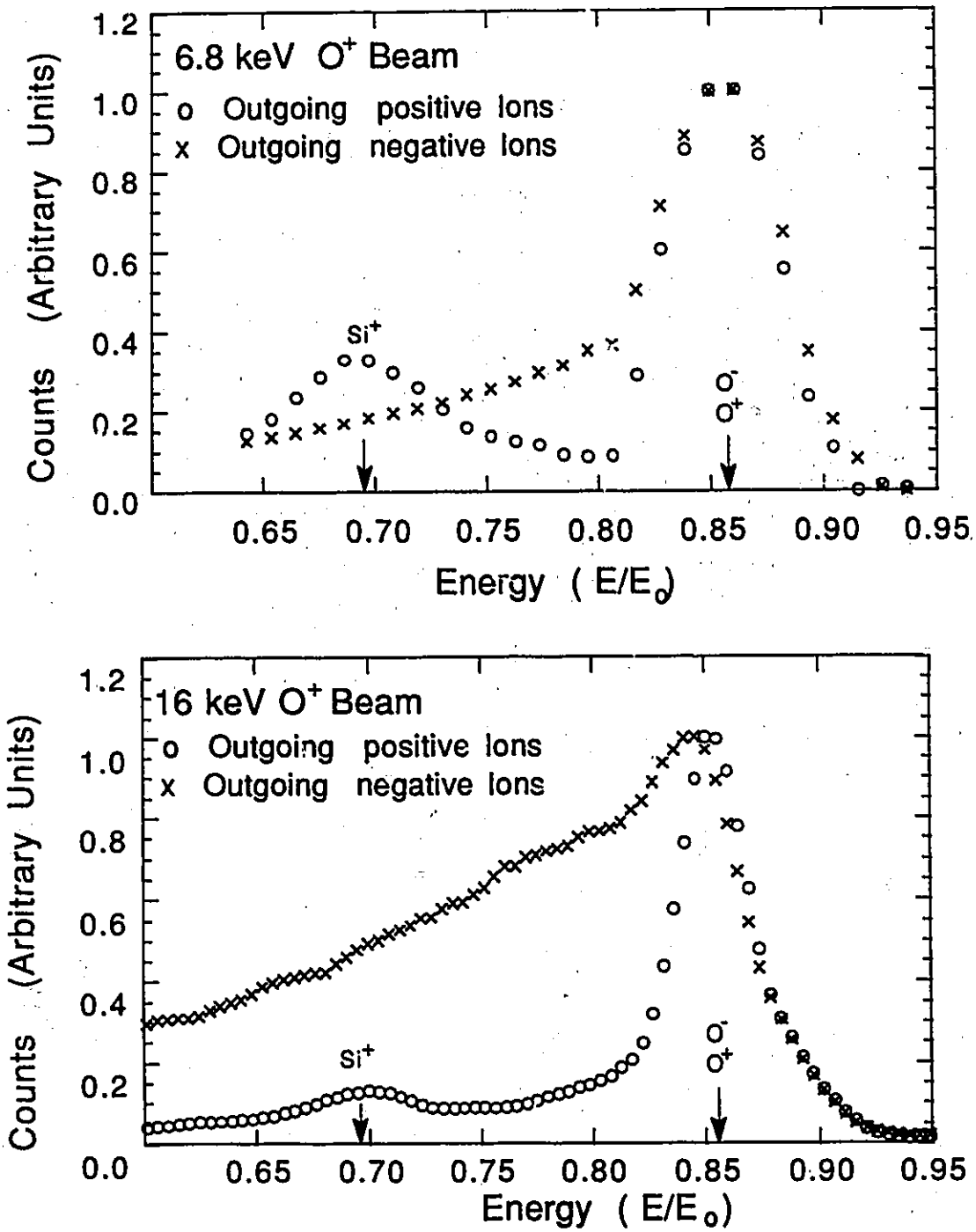

FIGURE #16 Energy spectra using 6.8 keV and 16.0 keV positive oxygen beams Using a negative oxygen beam under identical scattering conditions produced energy spectra which were indistinguishable from the two above.

Another interesting aspect is that the positive ion spectrum shows a surface recoil peak while the negative spectrum does not. This recoil atom was produced when an oxygen ion was scattered downwards into the surface and the recoiling silicon ion was emitted. The fact that it was not detected on the negative spectrum suggests that Si^- ions were not formed when silicon atoms left the surface. The shapes of the spectrums taken with both positive and negative primary ion beams were indistinguishable.

The positive and negative ion yields were again estimated from the peak areas. For the negative ion spectrum the inelastic continuum, which extends from lower energies into the lower energy side of the elastic peak, posed a slight problem which was resolved by fitting the maxima and the higher sides of the surface peaks. Since inelastic processes involved multiple collisions they were less likely to show the memory effect, so that this method of estimating the negative ion yield slightly diluted any memory effect. However because the shapes of these spectrums were indistinguishable for different sign incident beams, the effect on the negative/positive incident beam ratio was small.

In FIGURE #17, the abscissa is proportional to the interaction time of the ion with the surface and the circles are for a positive beam ion beam while the crosses refer to a negative ion beam. The absolute values of each of the ratios is estimated to an accuracy of about 20% but by comparing the two beams at any one

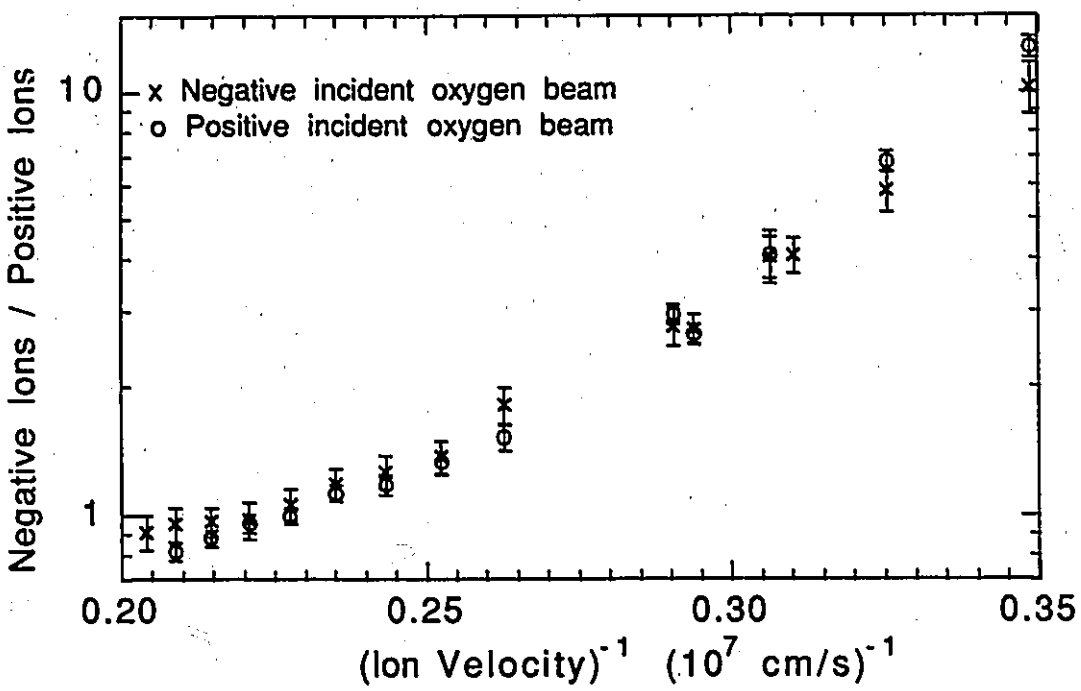

FIGURE #17 Ratio of outgoing negative ions to outgoing positive ions. The abscissa corresponds to ion beam energies between 19.9 keV and 6.8 keV.

energy the relative accuracy increases to about 5% to 10% and this is mostly the result of counting statistics. By examination of all the data we found the average of the ratio of the results at the same energy to be 1.021 ± 0.03. Within statistical error this is unity, so that our results strongly suggest that all memory of the initial charge state is lost for keV oxygen ions scattered from a silicon surface.

CHAPTER 6 - Conclusion

After several years of designing and building, the UHV system and the measurement apparatus are fully operational. Our efforts have produced a viable and versatile system. In particuliar, the RF type ion source produced a steady and well defined ion beam in the 6 to 20 keV range which allowed us to study our silicon sample using LEIS techniques. The commercial manipulator proved to be very efficient as did the electron beam heating accessory. The electrostatic analyser, which was designed and built here, proved to have the energy resolution predicted by the theoretical calculations.

Initial experiments have involved examining the crystal structure of a Si(100) sample using a 7 keV oxygen ion beam. By detecting the outgoing ions, a channeling and blocking spectrum was taken and the energy spectrum expected from a clean Si surface was obtained. Using our RHEED system confirmed that we indeed had the 2 x 1 crystal structure expected from the Si(100) surface.

In addition to this simple test, we gathered evidence that supported the widely accepted notion that an ion retains no information about it's initial charge state. Measurements of oxygen ions of both polarities surface scattered from silicon atoms, under conditions which favor binary collisions with individual surface atoms, were found to give the same ratio of negative to positive ion yields. Therefore this experiment provides strong evidence that keV oxygen ion scattered from a silicon surface lose all memory of their initial charge state.

APPENDIX I - Ultrahigh Vacuum procedures

Since surface studies are very critical of the surface cleanliness, the actual measurements had to be carried out in an UHV environment. Ultra-high vacuum is typically defined as a pressure less than 10^{-9} torr and the necessity of such vacuum for surface studies follows from the kinetic theory of gases which predicts a monolayer of molecules arrives at a surface in about 1 second at a pressure of 10^{-6} torr.

The procedure for going from atmospheric to UHV pressures required approximately 20 hours. The pressure in the chamber had to be at least in the low 10^{-2} torr range before it could be switched over to the diffusion pump. The chamber was equipped with a commercial diffusion pump that used a high grade oil called Santovac 5. This oil-diffusion pump was backed by a commercial rotary pump that was lubricated with a very good quality oil (Supergrade A supplied by Edwards Vacuum Systems). Within an hour of pumping, the pressure in the chamber was brought down to the low 10^{-6} torr range as measured on a UHV type ion gauge (for minimum X-ray background).

The next step was to bake the whole UHV chamber at a temperature of 120°C for about 8 hours. This heating removed most of the atmospheric contaminants covering the surfaces in the main chamber (thermal desorption). After a reasonable cooling down period (about 8 to 10 hours), the pressure fell in the low 10^{-9} torr range. The pumping speed of the diffusion pump was enhanced by providing liquid nitrogen cooling to its cold trap. Further pumping

speed was provided by a Titanium sublimation pump equipped with a cold plate which was also cooled with liquid nitrogen. Note that a sublimation pump has a good pumping speed for all gases except rare gases.

APPENDIX II - Cylindrical Electrostatic Analyser

Consider a cylindrical electrostatic field acting on an electron of mass m and charge -e which is projected into this field with an initial velocity v_0. The electric field intensity anywhere between the two cylindrical electrodes of radius r_1 and r_2 is represented by:

$$X = -\frac{A}{r} \qquad \text{where } r_1 < r < r_2$$

Here A is a constant which is determined by the boundary conditions on the electrodes. Using integration, this constant was found to be:

$$A = \frac{V_0}{\ln (r_2 / r_1)}$$

Note that $V_0 = (V_2 - V_1)$ which is the voltage between the electrodes (Figure #18).

The orbital analysis was solved by obtaining approximate solutions of the equation of the orbit. Starting with Lagrange's equation and assuming a central force:

$$\frac{\partial}{\partial t} \left(\frac{\partial L}{\partial \dot{q}}\right) - \frac{\partial L}{\partial q} = 0$$

In cylindrical coordinates q is r and ϕ, and the Lagrangian becomes

$$L = T - V = \frac{1}{2} m (\dot{r}^2 + r^2 \dot{\phi}^2) - V(r)$$

Lagrange's equation yields the differential equation of the orbit.

$$h^2 u^2 \left(\frac{d^2 u}{d\phi^2} + u\right) = \frac{Ae}{m} u$$

where $u = r^{-1}$ and h is the angular momentum per unit mass (this is a constant of the motion). If α denotes the angle between the optic axis and the initial direction of motion, then $h = r_o v_o \cos \alpha$. For simplification we introduce a dimensionless unit y ($= u / u_o$) and a parameter c defined by $c^2 = A e / (m v_o^2 \cos^2\alpha)$.

These substitutions simplify the differential equation to

$$\frac{d^2 y}{d\phi^2} + y = \frac{c^2}{y}$$

For paraxial trajectories where $y \rightarrow 1$ which start on the optic axis at $\phi = 0$ an approximate solution is of the form

$$y = c + (1 - c) \cos(W\phi) + b \sin(W\phi)$$

By substitution into the differential equation we obtain

$$b = - \tan \alpha / W \quad \text{with} \quad W = \pm \sqrt{2}$$

(the negative sign is the backward projection solution of the ray)

Thus the solution takes the form

$$y = c - \frac{\tan\alpha}{\sqrt{2}} \sin(\sqrt{2}\phi) + (1 - c) \cos(\sqrt{2}\phi)$$

The rays which diverge from the point source on the optic axis where $\phi = 0$ converge again to a spacial focus point on the optic axis where the tan α term is zero so that y becomes again the same for all α when

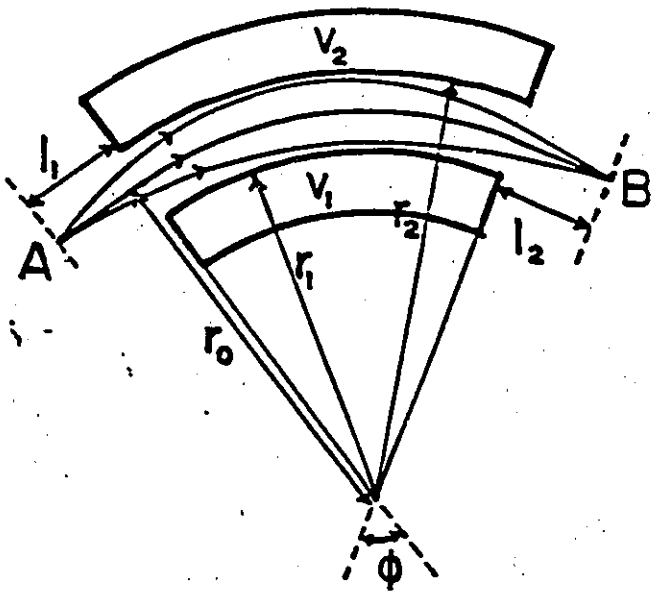

r_0 = 60.0 mm
r_1 = 58.0 mm
r_2 = 62.0 mm

FIGURE #18 Diagram denoting the parameters and the focussing lens action of the $\pi/\sqrt{2}$ ESA design. The thicker lines represent the ESA electrodes.

$$\sin(\sqrt{2}\,\phi) = 0$$

$$\sqrt{2}\,\phi = 0° \text{ or } 180°$$

$$\phi = (\pi / \sqrt{2}) \text{ radians} = 127°17'$$

Since the target formed the object of the analyser and it was much too large to fit between the electrodes, the theory was extended to find solutions such that the object point was placed in the electric field free region before the electrodes. Similarly the exit slit was also placed in the field free region beyond the electrodes. By reducing the deflection angle (ϕ) slightly, the focussing lens action is slightly less and the object and image points (A and B respectively) are further apart and are displaced to field free regions. For first order calculations, the relations are the same as for light optics and Newton's formula is applicable.

$$f^2 = (l_1 - g)\ (l_2 - g)$$

$$f = \frac{r_o}{\sqrt{2}\sin(\sqrt{2}\,\phi)} \qquad g = \frac{r_o}{\sqrt{2}}\cot(\sqrt{2}\,\phi)$$

assuming $l_1 = l_2$, then $f = \pm(l - g)$ or

$$l = g \pm f = \frac{r_o}{\sqrt{2}\sin(\sqrt{2}\,\phi)}\,(\cos(\sqrt{2}\,\phi) \pm 1)$$

The above equation is plotted in FIGURE #19.

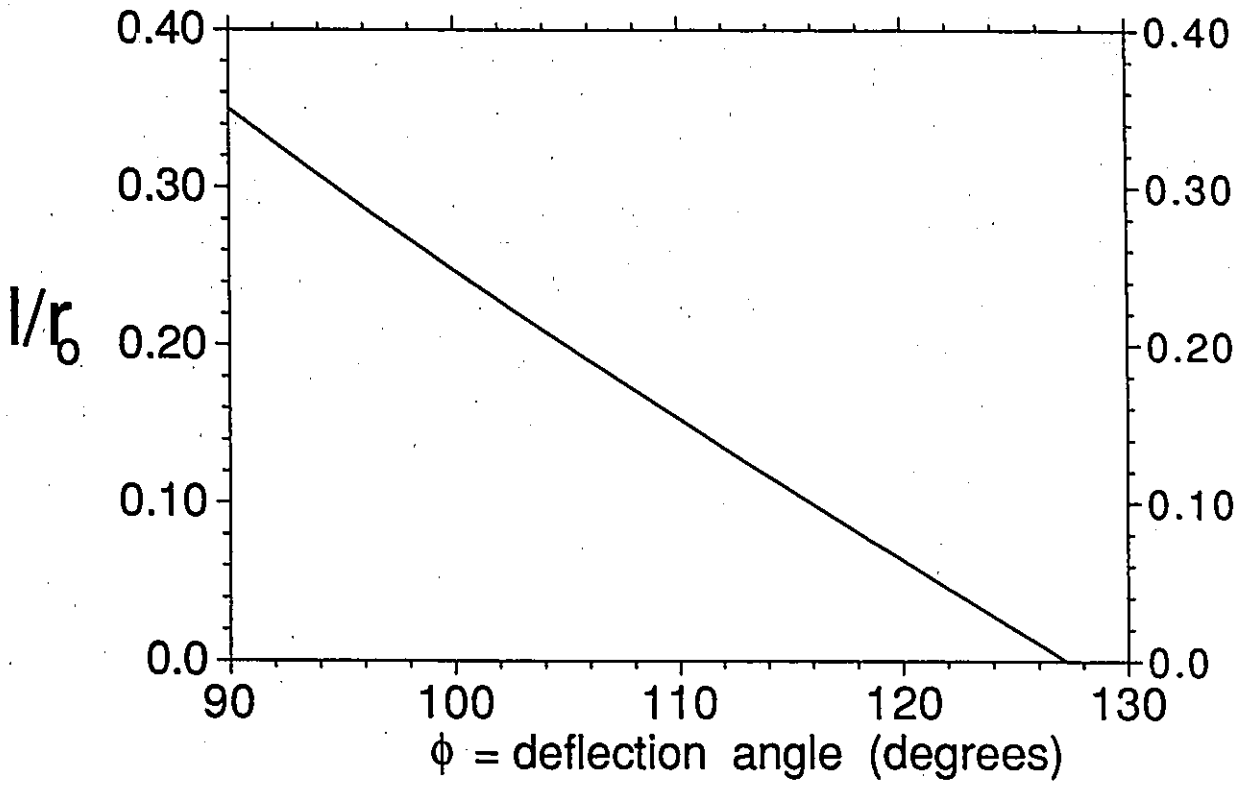

FIGURE #19 l/r_o versus deflection angle

REFERENCES

1. E. Taglauer and W. Heiland, Appl. Phys. 9, 261 (1976).

2. M. Aono, Y. Hou, C. Oshima and Y. Ishizawa, Phys. Rev. Letters. 49, 567 (1982).

3. M. Aono, C. Oshima, S. Zaima, S. Otani and Y. Ishizawa, Jpn. J. Appl. Phys. 20, L829 (1981).

4. C. H. Pattersen and T. M. Buck, Surf. Sci. 218, 431 (1989).

5. E. Everhart, G. Stone and R. J. Carbone, Phys. Rev. 99, 1287 (1955).

6. D. P. Smith, J. Appl. Phys. 38, 340 (1967).

7. E. P. Suurmeijer, A. L. Boers, Surf. Sci. 43, 309 (1973).

8. J. F. Van Der Veen, Surf. Sci. Rep. 5, 199 (1985).

9. M. Aono, Y. Hou, R. Souda, C. Oshima, S. Otani et al., Jpn. J. Appl. Phys. 21, L670 (1982).

10. K. Komaki and F. Fujimoto, Jpn. J. Appl. Phys. 21, L521 (1982).

11. B. Hird, Can. J. Phys. 69, 70 (1991).

12. J. Los and J. J. C. Geerlings, Phys. Rep. 190, 133 (1990).

13. R. Brako and D. M. Newns, Rep. Prog. Phys. 52, 655 (1989).

14. S. S. Schekter, J. Exp. Theo. Phys. (USSR) 7, 750 (1937).

15. J. W. Gadzuk, Surf. Sci. 6, 133 (1967); 6, 159 (1967).

16. E. G. Overbosch, B. Rasser, A. D. Tanner and J. Los, Surf. Sci. 92, 310 (1980).

17. R. P. N. Bronckers and A. G. J. Wit, Surf. Sci. 104, 384 (1981); Surf. Sci. 112, 111 (1981).

18. A. L. Hughes and V. Rojansky, Phys. Rev. 34, 284 (1929).

19. E. A. Wood, J. Appl. Phys. 35, 4 (1964).